Exploiting Polarimetric TerraSAR-X Data for Sea Clutter Characterization

Eduardo Makhoul, *Member, IEEE*, Carlos López-Martínez, *Senior Member, IEEE*, and Antoni Broquetas, *Member, IEEE*

***Abstract*—This paper presents a detailed characterization of sea/ocean clutter returns at X-band, imaged by TerraSAR-X (TSX) mission from the radiometric, statistical, and polarimetric standpoints. Different TSX data takes, covering the typical spaceborne incidence angle region (20°–45°), are analyzed: dual-polarized and experimental quad-polarized (quad-pol) data have been used. The thermal noise of the receiver for quad-pol data turns out to be an important limitation in the sea characterization from TSX, particularly at high incidence angles (above 36°), where low signal-to-noise ratios (SNRs) can impair the proper data distribution fitting and the polarimetric backscattering description. Statistical analysis shows large deviation from Gaussianity, indicating presence of texture, mainly in the small incidence region (20°–36°), with favorable SNR conditions. The different polarimetric features revealed contribution of nonpolarized scattering, related to the presence of breaking waves. This paper also proposes and evaluates an extension of the well-known X-Bragg model, named X2-Bragg (extended-extended Bragg), which properly accounts for the impact of thermal noise and sea clutter temporal decorrelation, due to the dual receive antenna acquisition mode. Such additional decorrelation sources, if not properly analyzed and accounted for in the physical-based model description, could lead to an incorrect interpretation of the polarimetric properties and the related erroneous geophysical parametric inversion from the real data. In this sense, the X2-Bragg proves its fitting to the experimental data, quantifying accordingly the presence of nonpolarized scattering in terms of the roughness parameter β_1.**

***Index Terms*—Non-Gaussian clutter, parameter estimation, radar backscattering coefficient, sea clutter, statistical analysis, synthetic aperture radar (SAR), SAR polarimetry, X-Bragg.**

I. Introduction

THE imaging capability of synthetic aperture radars (SARs), independent from daylight and weather conditions, represents a potential tool for globally monitoring the ocean. SAR is a very important forecast instrument in oceanography, allowing, among others, the retrieval of ocean wave spectrums [1] and the measurement of ocean or river current velocities [2]. Lately, the increase in vessel hijacking, as well as the need to control fishing and tanker polluting activities, demand remote sensing systems to properly monitor maritime traffic. SAR sensors with ground moving target indication (GMTI) capabilities are of great interest for ship surveillance [3].

Characterization and modeling of the sea clutter returns observed by SAR systems are of great interest for the accurate evaluation of future SAR missions imaging the sea. The availability of polarimetric SAR instruments, such as TerraSAR-X (TSX) or TanDEM-X (TDX), provides a unique opportunity to gather geophysical and biophysical information of the marine environment. This paper exploits different dual-pol (HH/HV[1]) and experimental quad-pol TSX data sets (covering 20°–45° of incidence angle) to perform a transversal (radiometric, statistical, and polarimetric) and compact study of the sea echo returns. To the authors' knowledge, such analysis has not been performed yet, exploiting the experimental quad-pol data from TSX.

The main stress of the study is to point out the different limitations that may be encountered when operating TSX, particularly in the quad-pol mode, where the dual receive antenna (DRA) mode is used [4], such that the antenna is split into two halves (receiving H and V simultaneously) and the transmit polarization is toggled in a pulse basis. On one hand, there is an increase of 3 dB in the noise equivalent sigma zero (NESZ) due to a reduced antenna effective area per channel, i.e., 3-dB loss in signal-to-noise ratio (SNR). On the other hand, a temporal lag exists between the different polarimetric channels, during which sea clutter decorrelates. The identification of such technological-driven aspects from the signal-based analysis proves to be of key importance in the correct interpretation of the polarimetric data when fitting physical-based models. In this sense, the X-Bragg model [5], which extends the Bragg surface scattering to include the impact of depolarized and cross-polarized returns, has been optimized to account for such additional perturbations (noise+sea temporal decorrelations), based on a comprehensive theoretical formulation, leading to the extended-extended Bragg (X2-Bragg) model; otherwise, these additional decorrelation sources could produce an erroneous interpretation of the polarimetric backscattering properties when trying to fit the physical-based X-Bragg model to the experimental data.

The radiometric analysis, in terms of the radar backscattering coefficient σ^0, shows that, in TSX, the thermal noise of the re-

Manuscript received April 24, 2015; revised July 9, 2015; accepted July 12, 2015. This work was supported in part by the FPU Research Fellowship Program, Ministerio de Educación under Contract AP2009-4590; by the FI-AGAUR Research Fellowship Program, Generalitat de Catalunya under Contract 2010FI EM051757; and by the Spanish Ministry of Science and Innovation (MICINN) under projects TEC2011-28201-C02-01 and TIN2014-55413-C2-1-P.

E. Makhoul was with the Department of Signal Theory and Communications, Universitat Politècnica de Catalunya, 08034 Barcelona, Spain. He is now with isardSAT, 08042 Barcelona, Spain (e-mail: edumak@tsc.upc.edu).

C. López-Martínez and A. Broquetas are with the Department of Signal Theory and Communications, Universitat Politècnica de Catalunya, 08034 Barcelona, Spain (e-mail: carlos.lopez@tsc.upc.edu; broquetas@tsc.upc.edu).

Color versions of one or more of the figures in this paper are available online at http://ieeexplore.ieee.org.

Digital Object Identifier 10.1109/TGRS.2015.2457242

[1]H and V refer to horizontal and vertical polarizations, respectively.

TABLE I
TSX DATA TAKES USED IN THE SEA CLUTTER CHARACTERIZATION (BW_R AND BW_A ARE RANGE AND AZIMUTH PROCESSED BANDWIDTHS, v_{win} AND θ_{win} ARE WIND SPEED AND DIRECTION FROM WHICH THE WIND IS BLOWING)

ID	Date	Region	Location	Mode	γ [deg]	BW_R [MHz]	BW_A [Hz]	v_{win} [m/s]	θ_{win} [deg]
TSX-1	05.03.2013	Senegal	N15.07-W17.60	Duad-Pol	19.85-21.74	150	1380	-	-
TSX-2	09.03.2013	Gulf of Guinea	N3.56-W2.35	Duad-Pol	22.43-24.26	150	1380	-	-
TSX-3	25.04.2010	Vancouver Island	N49.72-W127.97	Quad-Pol	23.75-25.49	150	1380	12.1	143
TSX-4	06.05.2010	Vancouver Island	N49.72-W127.97	Quad-Pol	23.75-25.49	150	1380	6.3	331
TSX-5	16.03.2013	Mauritania	N19.45-W16.78	HH	24.80-27.99	150	2765	-	-
TSX-6	30.04.2010	Bermuda	N31.37-W69.54	Quad-Pol	29.70-31.30	150	1380	6.5	258
TSX-7	11.05.2010	Bermuda	N31.37-W69.54	Quad-Pol	29.70-31.30	150	1380	6.9	62
TSX-8	05.03.2013	Mauritania	N18.78-W17.43	Dual-Pol	30.81-32.33	150	1380	-	-
TSX-9	05.03.2013	Senegal	N13.91-W18.48	Dual-Pol	31.91-33.42	150	1380	-	-
TSX-10	12.04.2010	Barcelona	N41.23-E2.11	Quad-Pol	33.04-34.50	150	1380	-	-
TSX-11	28.04.2010	Southeast Yakutat	N58.20-W137.96	Quad-Pol	36.18-37.54	150	1380	7.2	164
TSX-12	09.05.2010	Southeast Yakutat	N58.20-W137.96	Quad-Pol	36.18-37.54	150	1380	5.7	350
TSX-13	23.04.2010	Pratas Island	N20.67-E116.92	Quad-Pol	39.03-40.29	150	1380	-	-
TSX-14	25.04.2010	South Hecate Strait	N52.37-W129.81	Quad-Pol	40.02-41.25	150	1380	13.1	140
TSX-15	06.05.2010	South Hecate Strait	N52.37-W129.81	Quad-Pol	40.02-41.25	150	1380	6.7	318
TSX-16	17.03.2013	Gulf of Guinea	N0.24-E7.97	Dual-Pol	43.45-44.58	150	1380	-	-
TSX-17	21.04.2010	North Sea	N54.38-E7.05	Quad-Pol	44.37-45.48	150	1380	-	-

ceiver could be an important limiting factor for proper sea clutter characterization (statistical and polarimetric backscattering fitting), particularly in the case of quad-polarized acquisitions and for the spaceborne high-incidence region (36°–45°) due to the reduced SNR conditions. The σ^0 model, i.e., XMOD2 [6], optimized from TSX/TDX dual-pol data, provides a close fitting to the measured data also for the quad-pol case, where remaining calibration issues on the experimental DRA mode may induce additional errors [7].

The statistical analysis based on the computation of the normalized intensity moments (NIM) [8], and complemented by the log-cumulants' study [9], [10] confirms deviation from Gaussian statistics for the high-resolution X-band system [8], [10]–[13], and mainly at incidence angles below 36°, where sufficient SNR is available.

To evaluate the scattering properties of the sea when imaged by TSX, the polarimetric roll-invariant parameters, i.e., entropy H and mean scattering angle $\overline{\alpha}$ described in [14], as well as the polarization ratio (PR) metrics [10], [15], have been exploited. The results indicate that most of the acquisitions lie in the low to medium random surface scattering region, mainly due to the important contribution of nonpolarized returns, as indicated by $H/\overline{\alpha}$ and PR analyses. The proposed X2-Bragg model shows a good fitting with the experimental data in the $H/\overline{\alpha}$ plane, providing a mechanism to model the nonpolarized returns in terms of β_1 parameter, which is an indicator of the surface roughness (breaking waves events are known to cause an increase in surface roughness [8], [16]).

The remainder of this paper is organized as follows. In Section II, the TSX data set is presented. The methodology followed to perform the sea clutter characterization is introduced in Section III. In Section IV, the radiometric analysis in terms of radar backscattering coefficient is presented. Later on, the statistical description of the experimental data set is analyzed in Section V. To end up the transversal characterization, a complete polarimetric analysis is carried out in Section VI. Conclusions are drawn in Section VII. A comprehensive derivation of the proposed X2-Bragg model and its theoretical evaluation are considered in Appendixes A and B.

II. DATA SET DESCRIPTION

The main parameters of the stripmap products used in the analysis are summarized in Table I. The different data sets are made up of acquisitions from both the TSX and TDX instruments. Different aspects were considered for the selection of the data under analysis: 1) covering the spaceborne SAR operational range of incidence angles from 20° to 45°; 2) avoiding heterogeneity in the reflectivity over the imaged area; 3) avoiding regions with high density of maritime traffic and/or marine littorals (because of the high ambiguities' impact in the DRA acquisition); and 4) when possible, polarimetric acquisition is preferred over single polarization.

The available fully polarimetric TSX data were acquired during the experimental DRA mode campaign, April and May 2010. It is well known that sea or ocean conditions, and hence their radar response, could be quite different depending on the geographical location of the marine scenario under analysis; this is why it has been tried to sample the acquisitions over different oceans (Atlantic and Pacific) and seas (North, Mediterranean, and China). For the nominal dual-polarization stripmap products, the absolute and relative radiometric accuracies are 0.6 and 0.3 dB, respectively; whereas for the quad-polarization products, there is no specification, since it is an experimental mode with few dedicated campaigns and additional investigations on the DRA calibration issues need to be considered [7].

Portions of the images of three representative data takes (near/TSX-4, middle/TSX-7, and far range/TSX-17) are shown in Fig. 1; only copolarized channels (S_{HH} and S_{VV}) are considered since the cross-polar returns are corrupted by the thermal noise. Data takes TSX-4, TSX-7, and TSX-17 correspond, respectively, to high-, medium-, and low-SNR scenarios, with mean values of 16.3, 10.9, and 3.7 dB for the copolar S_{HH} channel. The average SNR estimated values are summarized in Table II for the different data takes, where the cross-polarized returns have low SNR (most of them around 1–5 dB). Data takes TSX-11 and beyond (incidence angle above 36°) have a higher impact of the thermal noise, as indicated by the reduced SNR conditions, even for the copolar channels. For TSX-4 [see Fig. 1(a) and (b)], the local surface wind produces an

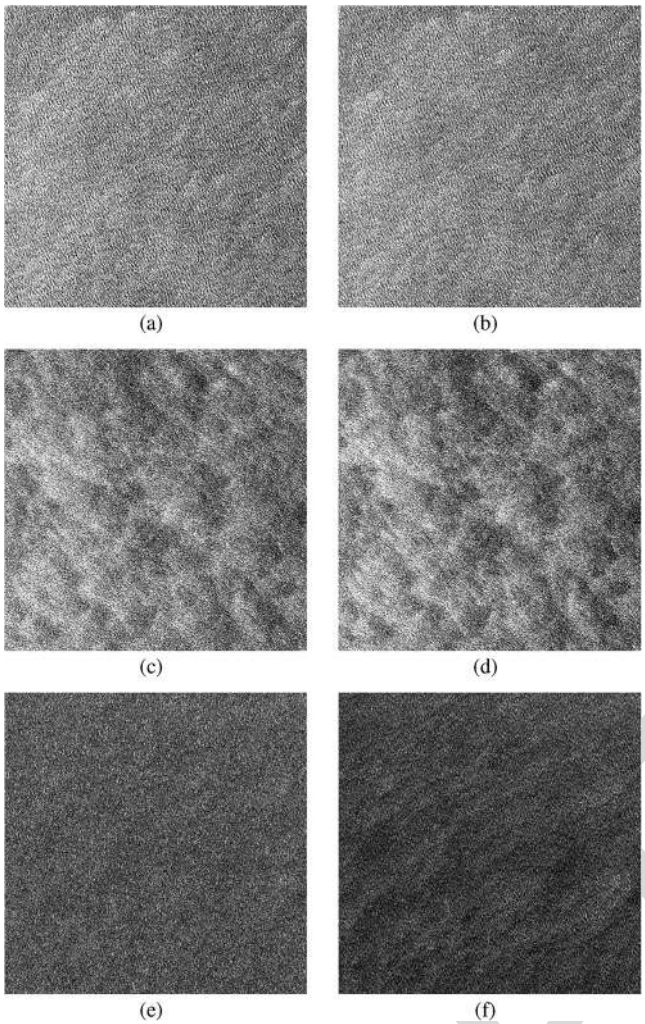

Fig. 1. Multilook (11 × 11) patches (512 × 512 pixels). (a) and (b) S_{HH} and S_{VV} for TSX-4 ($v_{\mathrm{win}} = 6.3$ m/s and $\theta_{\mathrm{win}} = 331°$). (c) and (d) S_{HH} and S_{VV} for TSX-7 ($v_{\mathrm{win}} = 6.9$ m/s and $\theta_{\mathrm{win}} = 62°$). (e) and (f) S_{HH} and S_{VV} for TSX-17 (no wind information).

TABLE II
ESTIMATED SNR AVERAGE VALUES FOR THE TSX DATA TAKES

ID	γ [deg]	SNR [dB]			
		S_{HH}	S_{VV}	S_{HV}	S_{VH}
TSX-1	19.85-21.74	23.0	-	4.8	-
TSX-2	22.43-24.26	19.6	-	4.3	-
TSX-3	23.75-25.49	17.7	17.9	6.8	6.9
TSX-4	23.75-25.49	16.3	16.5	5.9	6.1
TSX-5	24.80-27.99	11.7	-	-	-
TSX-6	29.70-31.30	8.7	9.9	3.8	4.0
TSX-7	29.70-31.30	10.9	11.6	4.2	4.3
TSX-8	30.81-32.33	9.2	-	4.0	-
TSX-9	31.91-33.42	9.1	-	4.1	-
TSX-10	33.04-34.50	6.5	8.6	0.9	1.3
TSX-11	36.18-37.54	5.1	6.6	2.6	2.6
TSX-12	36.18-37.54	5.3	6.2	3.2	3.3
TSX-13	39.03-40.29	6.4	8.9	2.8	3.4
TSX-14	40.02-41.25	5.8	8.8	2.6	3.4
TSX-15	40.02-41.25	3.5	4.5	2.5	2.4
TSX-16	43.45-44.58	2.8	-	2.2	-
TSX-17	44.37-45.48	3.7	6.2	2.3	2.4

appreciable wave pattern. For TSX-7 [see Fig. 1(c) and (d)], a more turbulent scenario is observed with a front propagating mainly in the diagonal direction. Turbulence, such as eddies or upwellings, could produce such response, bringing also some organic material (surfactants) to the surface [17]. At the highest incidence angle region, i.e., TSX-17, the HH channel has a noise-like pattern [see Fig. 1(e)] compared with VV [see Fig. 1(f)], where a wave pattern is roughly appreciated.

Ground truth data from the historical database of the National Data Buoy Center of the National Oceanic and Atmospheric Administration and the Canadian Moored Bouy of the DFO are available only for some acquisitions, as indicated in Table I. The geographical location of the employed buoys matches the center of the acquired images, but the temporal sampling rate is not sufficient to determine the exact sea conditions. Typical differences on time are between 30 and 60 min before or after the acquisition time; however, in most cases, sea conditions are quite stable in a 4-h window around the acquisition time.

III. SEA CLUTTER CHARACTERIZATION METHODOLOGY

A software module has been implemented to automatically perform a complete and exhaustive characterization of the data based on the three-level approach (radar backscattering coefficient,[2] statistics, and polarimetry). This analysis module can accept as input a set of different data takes from different sensors, where each is processed sequentially.

The first submodule performs a radiometric calibration, based on the input product information as described in [18], such that the intensity of the pixels at its output is related to σ^0 values.[3] In the next block, the area of interest (AOI) is selected, which is, to date, carried out simply by a visual inspection of the image product considering a rectangular AOI. Afterward, a subregion characterization based on a sliding window over this very AOI is performed. It is possible to define the size of such a sliding window and the overlapping in both range and azimuth dimensions.

For the statistical characterization and the normalized reflectivity σ^0 estimation, a window considering the whole azimuth strip for each range bin (range line basis) within the AOI has been selected. Therefore, the dependence of different descriptors with the incidence angle can be studied. For polarimetric decomposition, a rectangular sliding window of 11 × 11 without overlapping has been used to avoid mixing different scattering mechanisms and obtain adequate speckle filtering [19]. As proposed in [5], an additive noise filtering (NF) (for quad-pol data) can be performed in order to reduce the noise impact. Then, the polarimetric description is performed before and after NF.

Prior to sub-AOI dependent characterization, specific filtering on the data can be optionally completed,[4] such that the impact of man-made structures present in the open sea (such as vessels, oil platforms, and wind farms) is minimized, avoiding

[2]In the literature, the radar backscattering coefficient is also referred as normalized radar cross section (NRCS).

[3]It must be noted that those pixels with negative intensities, once the calibration is performed, are excluded from the subsequent characterization.

[4]This filtering method has been considered only for those data takes where a high density of high-reflectivity man-made targets is expected, based on a visual prescreening approach, taking into account the *a priori* geographical location of the region being analyzed; otherwise, and depending on the filtering threshold, the sea clutter data characterization could be impaired.

corruption of the data analysis. A simple filter approach has been implemented: those pixels, whose magnitude y_i

$$y_i \geq \mu_{\text{subAOI}} + \beta\sigma_{\text{subAOI}} \quad (1)$$

exceeds the mean statistical value μ_{subAOI} in a given number of times β the standard deviation σ_{subAOI}, are discarded. Both statistical moments are estimated from the available samples within the sub-AOI, whereas the β term is experimentally adjusted, with typical values between 2 and 6.

IV. Radiometric Analysis (NRCS)

Most of the available semiempirical models of σ^0 (NRCS) are optimized for the low grazing region, based on ground-based radar observations. Therefore, they are not applicable for spaceborne SAR acquisitions typically at 20°–45° of incidence angle. Recently, two models have been proposed: the first one, the Naval Research Laboratory (NRL) [20], is based on the Nathanson reference tables in [21], covering the region of 30°–90°; the second one, named XMOD2 [6], has been optimized from TSX/TDX copolar data, for incidence angles from 20° to 45°. XMOD2 provides σ^0 values at VV, and thus, PR models should be used to retrieve the HH component. In [6], three models (T-PR, E-PR, and X-PR) have been adjusted for copolarized TSX data.

The estimated σ^0 for the different data takes is depicted as a function of the incidence angle in Fig. 2 for the copolar channels. A sliding window in a range line basis is used, i.e., σ^0 is averaged using all the azimuth samples in a range bin. The sea return decreases as a function of incidence angle, where the S_{VV} channel has, in general, a higher backscattering than S_{HH}. Cross-polar channels, not reported due to space limitations, have low σ^0 values, close to noise level. NESZ is also reported for the different data takes as dotted black lines in Fig. 2, which can help in understanding the impact of the thermal noise on each data take and thus the related SNR metric (estimated average values are reported in Table II). Comparing the NESZ of quad-pol data with dual-pol acquisitions (e.g., TSX-6 versus TSX-8), a degradation around 3 dB is observed due to the DRA mode operation. Therefore, the increase on NESZ (or decrease in SNR) for quad-pol data will impair the proper characterization of the sea clutter using TSX data. For some data takes (e.g., TSX-11, TSX-12, TSX-15, and TSX-16), and due to their reduced SNR conditions (≈2–5 dB), the effect of the antenna elevation pattern at the edges of the corresponding subswath can be clearly appreciated.

In Fig. 2, the range of copolar values predicted by the NRL and XMOD2 models for a sea surface wind speed range of 0.1–20 m/s is indicated by the shaded regions, delimited by dash–dot–dot and dashed gray lines, respectively. In the XMOD2 case, an average of the upwind, crosswind, and downwind conditions has been considered. Moreover, the expected values for HH have been also averaged for the different PR models (T-PR, E-PR, and X-PR). For data takes with ground truth information, the NRL model has an average deviation w.r.t. the estimated values of 6.92 and 5.11 dB for S_{VV} and S_{HH} channels, respectively; whereas XMOD2 presents a mean error of 0.98 dB for S_{VV}; and for the S_{HH} channel, the average deviations are 1.12, 1.23, and 2.63 dB for T-PR, E-PR, and X-PR, respectively. This divergence between the VV and HH returns (also among the different PR models) has been observed when retrieving wind speeds from TSX/TDX VV-only data and HH-only data as noted in [6], exploiting XMOD2 and PR models.

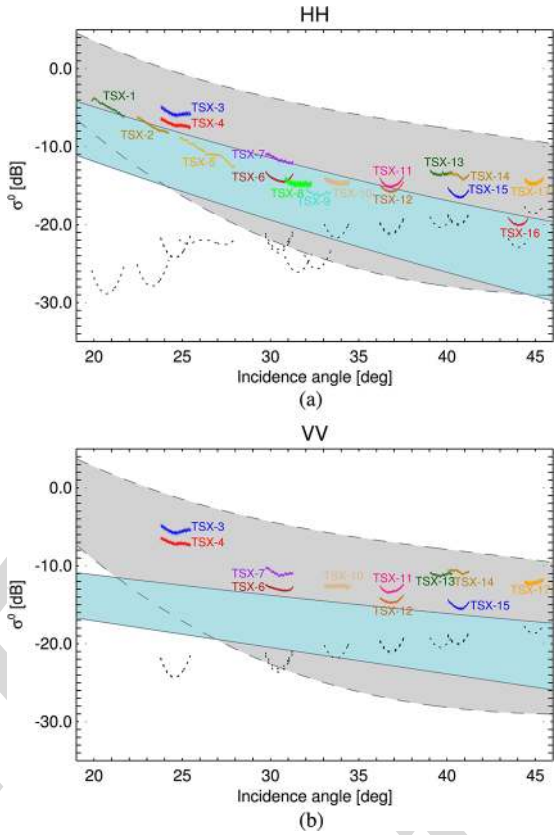

Fig. 2. Estimated σ^0 as a function of the incidence angle, using a sliding window in a range line basis with no overlap. (a) HH. (b) VV. The different data takes correspond to different colors; the (dotted black line) estimated NESZ is also plotted, and the shaded regions represent the predicted values from the NRL (delimited by dash–dot–dot lines) and XMOD2 (delimited by dashed lines) models, for a wind speed variation of 0.1–20.0 m/s (average value between upwind, crosswind, and downwind is performed for XMOD2 and an average over the different PR models for HH extraction).

Since the available information of the sea conditions does not correspond precisely to the time of acquisition, some error could be introduced in the inversion of σ^0 for the theoretical models. The NRL parametrization uses only two Nathanson tables [21], at 30° and 60° of incidence angle, whereas five tables are used to model reflectivity at incidence angles greater than 80° [20]. Therefore, a degradation in properly modeling σ^0 is expected when considering typical spaceborne geometries with 20°–45°.

In case of XMOD2, which agrees much better with the estimated values, the source of discrepancy should be also related to the fact that this model has been optimized for a given set of TSX/TDX copolarized acquisitions, not for quad-pol data. Moreover, the quality of such experimental data (DRA operation) should be carefully reviewed, particularly taking into account that some calibration issues have been highlighted when retrieving the fore and aft signals from the sum and difference ones [4]. The calibration procedure proposed in [4] has been applied for the along-track interferometric mode, where the receive polarizations of the two halves of the antenna

TABLE III
STATISTICAL DISTRIBUTIONS USED TO FIT THE SEA CLUTTER AMPLITUDE Y (REFERENCES TO THE ESTIMATION METHODS ARE INDICATED)

Distribution	Probability density function (PDF)	Parameters	Ref.
Log-normal	$p_Y(Y) = \frac{1}{Y\sqrt{2\pi\sigma^2}} \exp\left(-\frac{(\ln Y-\mu)^2}{2\sigma^2}\right)$	μ (location) σ (scale)	[12]
Weibull	$p_Y(Y) = \beta\frac{Y^{\beta-1}}{a^\beta} \exp\left(-\left(\frac{Y}{a}\right)^\beta\right)$	β (shape) a (scale)	[22]
K-distribution[1]	$p_Y(Y) = \frac{4b\frac{(v+1)}{2}}{\Gamma(v)} Y^v K_{v-1}\left(2Y\sqrt{b}\right)$	v (shape) b (scale)	[23] [24]

[1] $\Gamma(\cdot)$ is the gamma function and $K_n(\cdot)$ refers to the modified Bessel function of second kind and order n.

are the same, but no investigations have been made for the quad-pol case (different polarizations in the fore and aft halves). Hence, and as stated in the TSX product specification [7], the DRA specific instrument characteristics have to be further investigated for full calibration. From these results, it is clear that an optimization of the XMOD2 and different PR models is needed for quad-polarized data, using a wide data set with *in situ* buoy measurements and considering further efforts in instrument calibration for the fully polarimetric operation.

V. STATISTICAL ANALYSIS

For low-resolution radars and grazing angles typically above 10° (incidence angles less than 80), the amplitude (or magnitude) statistics of the sea returns have a "speckle"-like pattern [8], [11], i.e., Rayleigh distributed in amplitude. For higher resolution systems, the statistical description of the echo returns deviates from the Gaussian hypothesis, having a target-like response with more heavy-tailed distributions [8], [11]. This non-Gaussian clutter has been commonly described, among others, by log-normal and Weibull distributions [12], [13]. K-distribution, which provides also a good description of the sea clutter magnitude for high-resolution radars [8], [11], has been theoretically justified on the basis of the *compound model* [8].

Table III lists the probability density functions (PDFs) and the related parameters for the log-normal, Weibull, and K distributions. Y refers to the amplitude (absolute value) of the single-look ith polarimetric channel S_i (complex data), either S_{HH}, S_{VV}, or S_{HV} (polarization states in reception and transmission are indicated by the first and second subindexes, respectively).

Fig. 3(a) and (b) show the fitting of the considered distributions (K, Rayleigh, log-normal, and Weibull) to the S_{HH} channel's magnitude for data takes TSX-4 and TSX-17, respectively, which correspond accordingly to high-SNR (16.3 dB) and low-SNR (3.7 dB) scenarios. Only the results for a specific single sub-AOI are shown, i.e., in this case, the data distributions are computed using all the azimuth samples for a specific single range bin. The distributions are plotted on a semilogarithm scale, i.e., the clutter is expressed in decibels, which, for calibrated data, refers to σ^0 (theoretical distribution fitting and parametric estimation done in the linear domain).

For TSX-4, in the small incidence angle region, K-distribution (dotted blue line with circle markers) fits best the data distribution (solid red line), particularly in the distribution's tail. This is crucial, for instance, in GMTI operation, since the tail's shape determines the detection threshold for a given false alarm

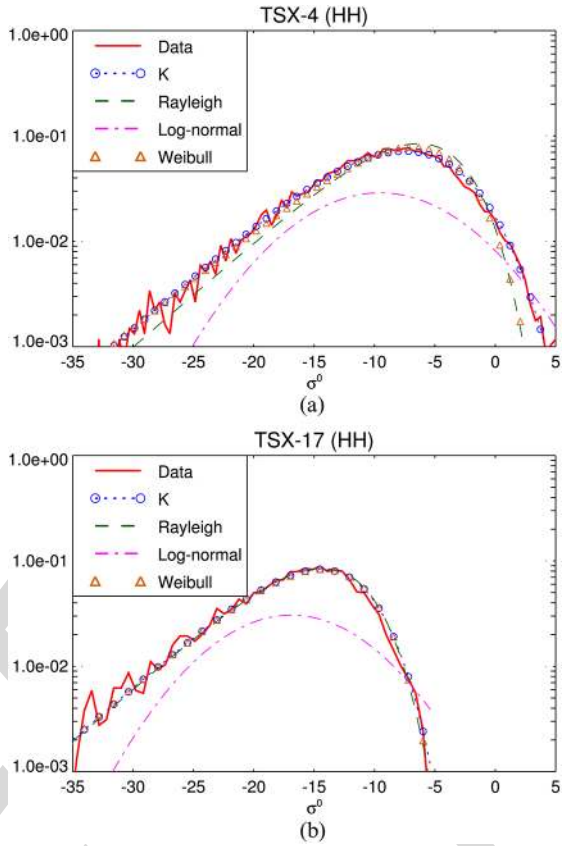

Fig. 3. Fitting of theoretical distributions (K, Rayleigh, log-normal, and Weibull) to the S_{HH} channel's magnitude (within a specific sub-AOI) for data takes (a) TSX-4 [SNR of 16.3 dB] and (b) TSX-17 [SNR of 3.7 dB].

rate. Weibull distribution shows good agreement with the data only for smaller σ^0 values, whereas the log-normal does not fit the data distribution. Similar results are obtained for the S_{VV} channel. In the cross-polar channel S_{HV}, the three distributions (K, Rayleigh, and Weibull) collapse to a complex Gaussian distribution mainly due to the noise impact. For TSX-17, the reduction in SNR, in comparison with TSX-4, leads to a major contribution of the thermal noise, which is translated into a more Gaussian-like data distribution. This behavior can be recognized from the statistical fitting in Fig. 3(b), where the K- and Weibull distributions tend to a Rayleigh one, i.e., shape parameters $v > 30$ and $\beta \approx 2$, accordingly. For the S_{VV} channel, there is an increase around 3 dB in SNR compared with HH polarization, and K-distribution slightly departs from Gaussianity, fitting best the data.

A good metric that allows deciding whether the data under analysis are spikier or tend to a Gaussian distribution is the shape parameter of the K-distribution, i.e., v. In Fig. 4, this parameter is shown as a function of incidence angle for the different data takes and copolar channels.[5] Blacknell's method has been used to estimate the shape and scale parameters of the K-distribution. Similar results have been obtained using the *fractional moments* method [23].

In the S_{HH} channel [see Fig. 4(a)], and for incidence angles between 20° and 33°, the shape parameter v has a range of

[5]For those data takes at incidence angle above 35° and with reduced SNR, only TSX-13 and TSX-14 are shown in Fig. 4 for clarity in the representation.

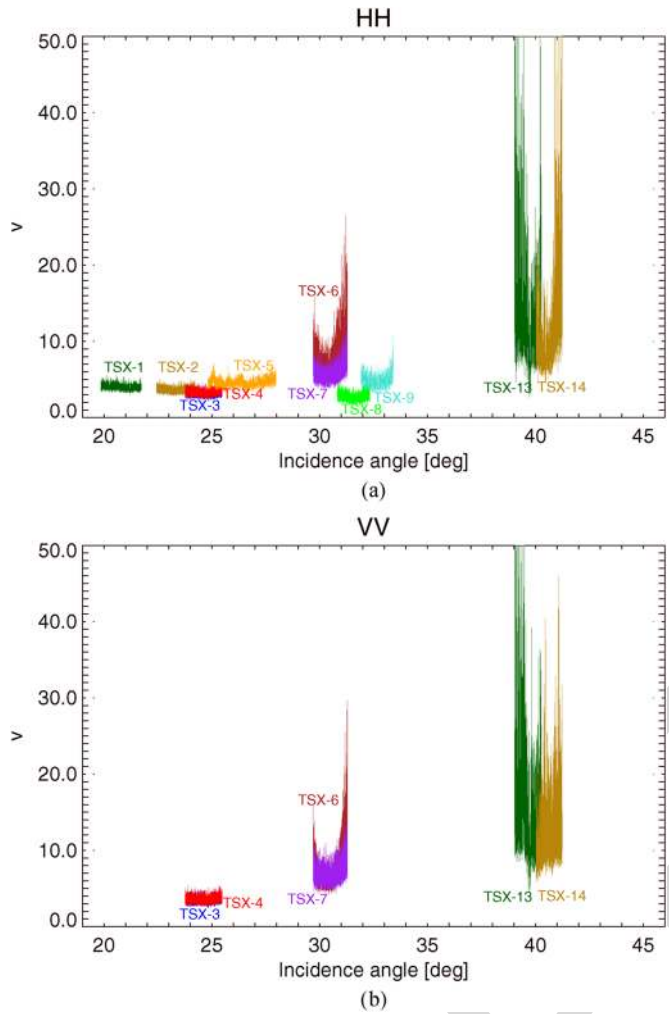

Fig. 4. Estimated shape parameter for a K-distributed amplitude fitting of the data as a function of the incidence angle, using a sliding window in a range line basis with no overlap. (a) HH. (b) VV. The different data takes are color-coded as in Fig. 2 (shape parameter estimated using Blacknell's approach).

3–10, with contained variation for each data take. For incidence angles greater than 36°, the values of the shape parameter are above 10, with much higher dispersion, related to the reduction in SNR as incidence angle increases [see Fig. 2(a) and Table II]. This is quite evident for TSX-16 and TSX-17, where noise impact produces a variation on the shape parameter from 10 to 1000. For VV polarization [see Fig. 4(b)], similar trends are observed, but in this case, the higher sea clutter returns in the high incidence region reduce the shape parameter dispersion on data take TSX-17, with values between 5 and 20. Comparing the shape parameters of the polarimetric channels, different values are obtained showing that the scalar product model (on which K-distribution is based) can be extended to a multivariative product model, associating an individual texture variable per polarimetric channel. For the cross-polar channels, high values of the shape parameter are obtained with a high dispersion due to the low sea backscattering contribution (close to NESZ).

One way to quantitatively evaluate the non-Gaussian behavior of the data is by computing the NIM of the nth order [8], i.e.,

$$\mathrm{NIM}_n = \frac{E\{Z^n\}}{E^n\{Z\}} \tag{2}$$

where Z refers to data intensity (or power), i.e., $Z = Y^2$, being $Y = |S_i|$ the magnitude, and $E\{\cdot\}$ is the expectation operator. Values of the nth-order NIM above $n!$ (Gaussian limit) are indicators of spiky data.

In general, and for the copolar channels, the estimated NIM (as a function of the estimated K-distribution shape parameter v) follows quite good the theoretical K-distribution NIM trend, for the third and fourth orders, when considering small to medium values of v (< 10), i.e., spikier clutter returns. Therefore, the compound model theory that supports the K-distribution is able to describe the mechanism, which results from a combination of Bragg scattering (from resonant capillary waves) and whitecap scattering originated from breaking waves [8]. The presence of the latter phenomena is known to increase the spikiness of the clutter returns [8], associated to smaller values of v as observed for data takes with incidence angle below 30°, with medium to high SNR conditions (> 10 dB), as indicated in Table II.

Analogously, the estimated third- and fourth-order NIM have been compared with the theoretical ones for Weibull and log-normal distributions. Weibull presents, generally, a worse matching with the theoretical trends for the copolar channels compared with the K-distribution. When considering a log-normal distribution fitting, a very poor matching between the estimated NIM and the theoretical ones is obtained. In summary, K-distribution provides good fitting for specific TSX acquisitions over the sea, particularly for low incidence angles, where SNR conditions are favorable (> 10 dB). In this region, the lowest values of the K-distribution shape parameter are obtained, indicating a much spikier behavior of the data, which can be also related to the higher contribution of breaking wave events, as analyzed in Section VI.

K-distribution is among one of the statistical distributions used to model and describe non-Gaussian statistics, based on the well-known compound model. Under this hypothesis, the complex signal can be characterized as a product between the square root of a random variable T (representing the texture) and an independent zero-mean complex Gaussian random process ("speckle"). In this sense, the computation of the so-called *log-cumulants* is very useful to evaluate the presence of texture, i.e., non-Gaussian statistics [9]. Such analysis is typically performed through the log-cumulant diagram [9], [10], where the second κ_2 (variance) and third κ_3 (skewness) log-cumulants are plotted against each other. These *log-moments* are computed as [10]

$$\begin{aligned} \kappa_2 &= m_2 - m_1^2 \\ \kappa_3 &= m_3 - 3m_1m_2 + 2m_1^3 \end{aligned} \tag{3}$$

where m_n is the log-moment of order n, i.e., $m_n = 1/L \sum_{l=1}^{L} (\log Z_l)^n$, where L intensity samples have been used.

Fig. 5 shows the log-cumulant diagram for the three representatives acquisitions considered in Fig. 1 (from near to far incidence angle regions). These plans are covered by five (texture) distribution families, namely, Gamma (dash–dotted line modeling a K-distribution in amplitude), inverse Gamma (dashed black line), Beta (light gray shaded region), inverse

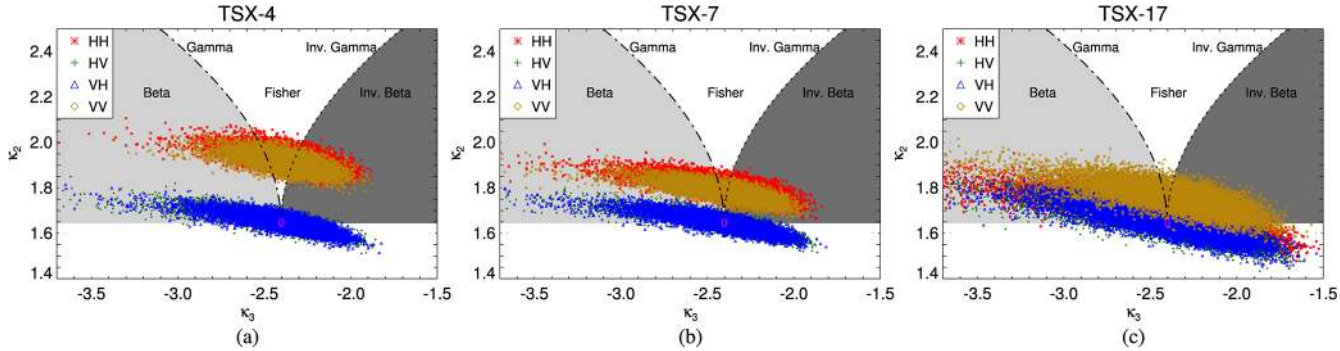

Fig. 5. Log-cumulant diagrams for different data takes: (a) TSX-4, (b) TSX-7, and (c) TSX-17. A sliding window in a range line basis with no overlap has been used (HH as red "x," HV as green "+," VH as "△," and VV as gold "◇").

Beta (gray shaded region on the right), and Fisher (region in between). The intersection point between these distributions corresponds to no texture at all, i.e., Gaussian statistics.

The results in Fig. 5 are in line with the previous statistical analysis: for TSX-4, in the near incidence angle region, the copolar channels lie higher up in the diagram compared with the cross-polar channels, indicating a deviation from Gaussian statistics (spikier response). As the incidence angle increases, the copolar channels move to lower regions in the diagram (less texturized). For TSX-17, with the highest incidence angle, VV has more texture compared with HH, as expected from the K-distribution shape parameter study.

VI. Analysis of the Polarimetric and Scattering Features

A. SAR Polarimetry

A polarimetric SAR (PolSAR) system measures the scattering matrix, which, for the monostatic case and on the Pauli basis, can be expressed in vectorial notation as

$$\mathbf{k} = \frac{1}{\sqrt{2}}[S_{\mathrm{HH}} + S_{\mathrm{VV}} \quad S_{\mathrm{HH}} - S_{\mathrm{VV}} \quad 2S_{\mathrm{HV}}]^T \tag{4}$$

where $(\cdot)^T$ refers to the transpose operator, and S_i are the complex data of the ith polarimetric channel. The distribution of $\mathbf{k}$ is completely described by the Hermitian positive definite coherency matrix $\mathbf{T} = E\{\mathbf{k}\mathbf{k}^H\}$ under the Gaussian assumption [25], where $(\cdot)^H$ is the transpose and complex conjugate operator.

The coherency matrix $\mathbf{T}$ is estimated from the data, such that the speckle noise is filtered. The maximum-likelihood estimator can be obtained as a spatial averaging (boxcar or multilook filter)

$$\widehat{\mathbf{T}} = \frac{1}{L}\sum_{i=1}^{L} \mathbf{k}_i \mathbf{k}_i^H \tag{5}$$

where L refers to the number of looks or samples employed in the estimation of $\mathbf{T}$, and $\mathbf{k}_i$ is the vector in the Pauli basis for the ith sample.

B. Features Definition

The main objective of the polarimetric study is to analyze the scattering properties of the sea surface observed by the high-resolution X-band TSX sensor. This way, two different sets of polarimetric features are considered. First, the eigendecomposition of the coherency matrix allows extracting roll-invariant parameters, such as the entropy H, anisotropy A, and mean alpha angle $\overline{\alpha}$, as originally proposed by Cloude and Pottier [14]. H measures the randomness of the scattering mechanism, $\overline{\alpha}$ provides physical information about the type of average scatter, and A (complementary to H) measures the relative significance of the second and third eigenvalues. The $H/A/\overline{\alpha}$ features allow a physical interpretation of the PolSAR data, and thus, their correct estimation provides a reliable prediction of physical parameters [5], [14]. This eigendecomposition-based analysis has been successfully applied over the oceans to determine polarimetric scattering mechanisms and for discrimination/classification of different types of slicks [16], [26], [27].

To complement the eigendecomposition-based analysis, additional polarimetric features exploiting the intensity of the copolarized channels have been used, based on the σ^0 model proposed by Kudryavtsev *et al.* [15]. As analyzed in [15], [28], and [29], the Bragg theory is not fully able to explain and represent the backscattering from the ocean, due to the existence of sea spikes (in high-resolution radar data), which induce large deviations of observed PR compared with the theoretical Bragg one. This suggested that some mechanism supporting non-Bragg scattering and connected with breaking waves also contributes to the NRCS from the sea. The proposed NRCS model in [15] is a superposition (in linear units) of a regular sea surface, polarized component related to the Bragg scattering (σ_{pp}^{0B}), and surface areas with enhanced roughness produced by breaking waves, nonpolarized component linked to non-Bragg scattering (σ_{pp}^{0nB}), i.e., $\sigma_{pp}^{0} = \sigma_{pp}^{0B} + \sigma^{0nB}$. It is assumed that the nonpolarized component is the same for both copolar channels.

As anticipated by several studies [15], [28], [29], the contribution of the nonpolarized radar returns to the total NRCS can be considerable, mainly due to the presence of breaking waves. As suggested in [15] and [29], the computation of the PR

$$\mathrm{PR} = \frac{\sigma_{\mathrm{HH}}^{0}}{\sigma_{\mathrm{VV}}^{0}} = \frac{\sigma_{\mathrm{HH}}^{0B} + \sigma^{0nB}}{\sigma_{\mathrm{VV}}^{0B} + \sigma^{0nB}} \tag{6}$$

is an indicator of the presence of significant wave breaking (PR ≈ 1), deviating from the PR for the Bragg component $p_B = \sigma_{\mathrm{HH}}^{0B}/\sigma_{\mathrm{VV}}^{0B}$. In this paper, p_B is computed as the ratio

between the perpendicular ($B_\perp$) and parallel ($B_\parallel$)[6] Bragg scattering coefficients according to [5]. It must be noted that the effect of slope of the long tilting waves on the NRCS is higher at the HH polarization than in VV, particularly at large incidence angles [15], and hence, this could lead to an increase in PR not directly related to the breaking waves. Nevertheless, it is complicated to separate the effect of breaking waves from tilting waves, since, in the formation process of the former ones, there is a progressive increase of the slope (generation of a sloping wave front) correlated with a temporal increase of the surface roughness [16]. In this sense, further studies are required to carefully analyze the impact of both tilting and breaking waves, trying to separate both processes.

C. X-Bragg and Extended X-Bragg (X2-Bragg) Models

It has been generally assumed that the radar sea echo returns are mostly dominated by Bragg surface scattering; however, some depolarization has been observed, as noted in [16], [26], and [30]. Such nonpolarized returns have been found to significantly contribute to the sea backscattering due to breaking waves (increasing surface roughness), as analyzed in [15], [28], and [29], particularly when increasing the frequency of operation (and thus the resolution) [15].

Under these considerations, the application of the small perturbation model (SPM) for the polarimetric scattering analysis would be too simplistic, as its validity range is limited to small surface roughness conditions [5]. Therefore, the evaluation of the X-Bragg model, originally proposed by Hajnsek *et al.* [5], seems to be more reasonable, since it is a two-component model, including a Bragg scattering term and a roughness induced rotation symmetric disturbance. This way, depolarization (nonpolarized components) and cross-polarized backscattering effects are included. As proposed in [5] and [16], this can be obtained modeling the surface as a reflection symmetric depolarizer, randomly rotating the Bragg coherency matrix $\mathbf{T}$ about an angle β w.r.t. the local surface normal and averaging it over a statistical distribution $p_\beta(\beta)$. For a uniform distribution $p_\beta(\beta)$ with zero mean and width β_1, the coherency matrix can be expressed by [5]

$$\mathbf{T} = m_s^2 \begin{bmatrix} C_1 & C_2\mathrm{sinc}(2\beta_1) & 0 \\ C_2^*\mathrm{sinc}(2\beta_1) & C_3\,(1+\mathrm{sinc}(4\beta_1)) & 0 \\ 0 & 0 & C_3(1-\mathrm{sinc}(4\beta_1)) \end{bmatrix} \tag{7}$$

where m_s is the backscatter amplitude related to the surface roughness; sinc function refers to $\mathrm{sinc}(x) = \sin(x)/x$; and the coefficients C_1, C_2 and C_3 can be expressed in terms of $B_\perp$ and $B_\parallel$ [5]. These coefficients depend on the incidence angle γ and the dielectric constant $\epsilon = \epsilon' - \jmath\epsilon''$. The latter can be obtained from the model developed by Klein and Swift [31].

The width of the distribution β_1 models the roughness disturbance of the surface and controls the level of cross-polarized power and the polarimetric $(S_{\mathrm{HH}} + S_{\mathrm{VV}})(S_{\mathrm{HH}} - S_{\mathrm{VV}})$ coherence [5]: for $\beta_1 = 0^\circ$ (smooth surface), the cross-polarized power is zero, and there is no depolarization effect (corresponding to the "pure" Bragg or SPM model); with increasing β_1 (increasing roughness), the HV term increases, and the $(S_{\mathrm{HH}} + S_{\mathrm{VV}})(S_{\mathrm{HH}} - S_{\mathrm{VV}})$ coherence decreases until 0 in the high roughness limit case of $\beta_1 = 90^\circ$ (azimuthally symmetric surface). The breaking waves produce a temporal increase in the surface roughness [8], [16], and this could be related to an increase also in the β_1 term of the X-Bragg model. In fact, this model has been used to derive a description of the polarimetric behavior of a breaking wave, as presented in [16]. Therefore, it is interesting to evaluate the applicability of the X-Bragg model to SAR polarimetric sea data, which can be useful for future studies trying to invert some geophysical parameters of the ocean using polarimetric data.

[6]Note that, here, perpendicular and parallel are referenced w.r.t. the incidence plane.

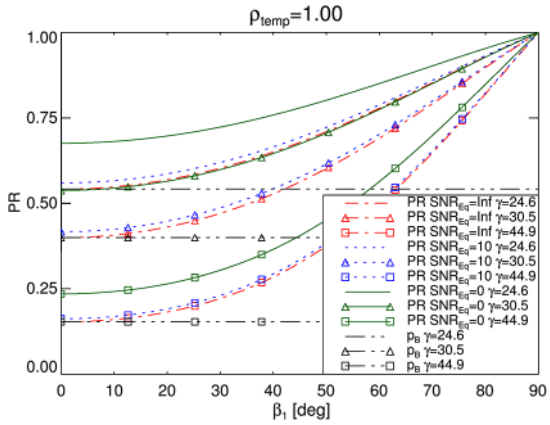

Fig. 6. PR of the X-Bragg ($\mathrm{SNR_{Eq}} = \infty$) and X2-Bragg models is represented as a function of the roughness β_1 parameter for different incidence angles γ and different noise conditions $\mathrm{SNR_{Eq}}$ (an X-band system at 9.65 GHz, a sea temperature of 10 °C, and salinity of 35‰ are considered).

The DRA acquisition mode [4], employed to obtain fully polarimetric images with an along-track interferometric configuration, has a two-folded impact on measured data. On one hand, as the receive antenna is halved, a direct consequence is a reduction on the received gain, which translates into higher values of NESZ. On the other hand, the alternate transmission of horizontal and vertical polarizations in a pulse-by-pulse basis jointly with the along-track configuration (to receive simultaneously H and V) produces a temporal lag between different pairs of channels. The different polarimetric channels should be spatial aligned (coregistered), such that they observe the scene from the same positions but at different times. During this time lag, around $\tau_{\mathrm{coreg.}} = 1$ ms for TSX S_{HH} and S_{VV} channels (or S_{HV} and S_{VH}), the sea backscattered field decorrelates due to internal clutter motion. Typical decorrelation times of the sea are between 8 and 10 ms for wind speeds of 15 m/s down to 5 m/s, [32]. For an X-band system at VV, the temporal coherence ρ_{temp} could be between 0.9 and 1.0 for a time lag around 1 ms, [32]. From the results presented in Section VI-D for TSX quad-pol, it has been observed that both the noise level and the sea clutter temporal decorrelation should be accounted for in the X-Bragg model to properly characterize the sea clutter in polarimetric terms. Taking into account these issues, the X-Bragg model has been extended to the X2-Bragg model (extended-extended Bragg). The mathematical derivation of the X2-Bragg

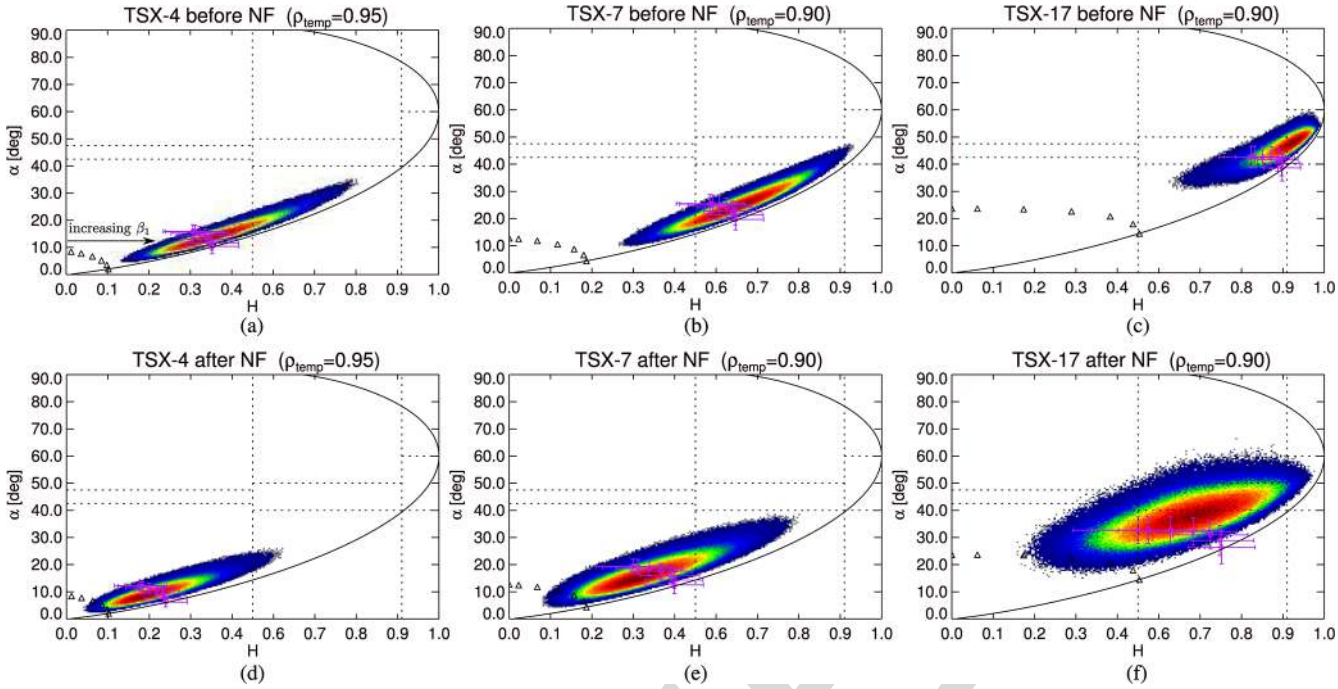

Fig. 7. Two-dimensional distributions on $H/\overline{\alpha}$ plane for different data takes (TSX-4, TSX-7, and TSX-17, from left to right), including the theoretical X/X2-Bragg models (β_1 variation from 0° to 90° and single dielectric constant for standard sea conditions of 10 °C and salinity of 35‰); black triangles refer to the original X-Bragg model, and magenta diamonds correspond to the X2-Bragg model (error bars/standard deviations in $H/\overline{\alpha}$ are included): (a)–(c) before and (d)–(f) after NF. (a) and (b) TSX-4 with $\rho_{\mathrm{temp}} = 0.95$. (b) and (e) TSX-7 with $\rho_{\mathrm{temp}} = 0.90$. (c) and (f) TSX-17 with $\rho_{\mathrm{temp}} = 0.90$.

and a theoretical evaluation for different system/scenario conditions are presented in Appendixes A and B, respectively.

In Fig. 6, the PR of the X-Bragg ($\mathrm{SNR_{Eq}} = \infty$) and the X2-Bragg is plotted as a function of β_1 for different incidence angles γ and effective[7] signal-to-noise ratio $\mathrm{SNR_{Eq}}$ conditions (no temporal decorrelation has been considered). The horizontal lines correspond to the PR for Bragg components p_B. It can be seen how the PR approaches p_B for β_1 close to zero (pure Bragg) and increases to higher values as roughness condition increases, with a value of 1 for complete depolarized scattering. From [15] and [29], this trend can be related to higher contribution of breaking wave events, which induce higher roughness conditions. It must be also noted that, as the noise contribution increases, there is also an increase in the PR, since the noise is a common nonpolarized term affecting both copolar channels.

D. Experimental Results

An analysis of the scattering plots in the $H/\overline{\alpha}$ plane has been carried out for the different data takes, without and with additive NF as proposed in [5]. Fig. 7 shows these 2-D distributions for the three representative data takes (near to far incidence, from left to right). Before NF, the dominant mechanism moves from low entropy surface scattering[8] at near incidence [see Fig. 7(a)], passing by medium entropy surface scattering [see Fig. 7(b)], ending up to high entropy region characterized by random anisotropic scatters [see Fig. 7(c)], caused by the higher noise contribution. Comparatively, NF produces a reduction both in H and $\overline{\alpha}$, leading to a dominant scattering in the low entropy surface zone ($H < 0.5$ and $\overline{\alpha} < 40°$) for data takes with incidence angle below 36° (e.g., TSX-4 and TSX-7).

The distributions of the eigenvalues in Fig. 8 for the three reference data takes are a good visual indicator of the polarimetric mechanisms' evolution as a function of incidence angle. In Fig. 8, the lowest eigenvalue (λ_4) has been also included since it provides information on the expected noise floor, such that the dominant mechanism's relative contribution with respect to the noise can be easily tracked. For TSX-4 [see Fig. 8(a)], there is a clear dominant mechanism (λ_1), surface scattering, as observed from the α_1 distribution in Fig. 9(a), centered around 5°. As incidence angle increases, the first eigenvalue decreases. At the farthest available incidence angle (TSX-17) [see Fig. 8(c)], no clear dominant mechanism is present, being the distributions of the eigenvalues closer to each other, such that a noise-like mechanism is expected in accordance with the σ^0 and statistical characterizations.

In general, the second mechanism almost keeps its relative strength w.r.t. noise floor independently of incidence angle. In Fig. 9, where the distributions of the individual α parameters are shown, the related α_2 with a similar trend as α_3 lies between 70° and 90°. These values are representative of double-bounce scattering, less probable in the sea backscattering. Considering the X-Bragg model extension to account only for thermal noise impact, parameters associated to the second mechanism do not agree with the observations from experimental data: on one hand, α_2 corresponds to 90° independently from β_1 and $\mathrm{SNR_{Eq}}$; on the other hand, the expected level of λ_2 is much closer to λ_3 than that observed from real data. These considerations reinforce the need to include also the impact of sea clutter temporal decorrelation between the polarimetric

[7]Please refer to Appendix A for further details on the definition of this equivalent $\mathrm{SNR_{Eq}}$.

[8]This region corresponds to zone 9 as designated by Cloude and Pottier [14], including surface scattering and specular scattering phenomena.

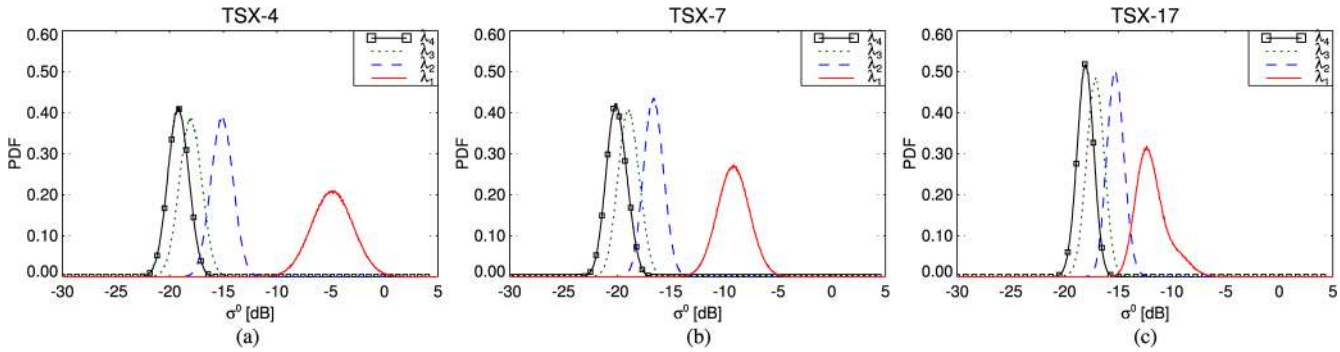

Fig. 8. Distribution of the eigenvalues, before NF, for different data takes. (a) TSX-4. (b) TSX-7. (c) TSX-17.

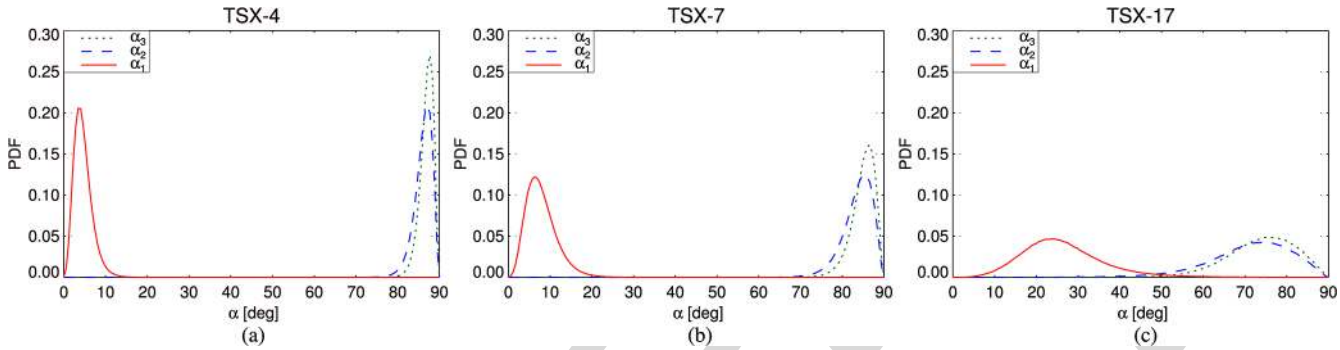

Fig. 9. Distribution of the alpha parameters, before NF, for different data takes. (a) TSX-4. (b) TSX-7. (c) TSX-17.

channels (ρ_{temp}), intrinsically related to the DRA acquisition mode itself, as proposed in the X2-Bragg model and described in Appendixes A and B.

On top of the different $H/\overline{\alpha}$ distributions in Fig. 7, the classical X-Bragg model, as black triangles, and the extended model X2-Bragg, as magenta diamond symbols, are depicted for different values of β_1 (from 0° to 90° in steps of 15°). Standard deviations are also included for the X2-Bragg model (related to SNR_{Eq} estimation from the data). Standard sea conditions have been assumed, i.e., 10 °C and 35‰ salinity.

An important bias exists between the original X-Bragg model and the data, after and, in particular, before NF. For X2-Bragg, a much better matching between the theoretical model and the experimental data is obtained. For TSX-4 [see Fig. 7(a)], a ρ_{temp} of 0.95 provides a good matching between the theoretical extended model and the data before NF, whereas for TSX-7 [see Fig. 7(b)], this value reduces to 0.90. In case of TSX-17 [see Fig. 7(c)], a higher bias is recognized, and reducing ρ_{temp} below 0.9 does not provide any additional improvement: from the theoretical analysis of the X2-Bragg model, higher clutter decorrelation does not increase entropy for regions with $H > 0.6$. Additive noise subtraction reduces entropy from 0.92 to 0.7, but the proposed extended model predicts an average alpha value below the one observed in the data. Therefore, there might be an additional mechanism contributing to this discrepancy, which is not considered in the X-Bragg model; additional measurements with higher SNR conditions should be analyzed to support this hypothesis.

The X2-Bragg model gets close to the centroid of the data distributions in $H/\overline{\alpha}$ for values of β_1 different from zero, which means that no pure Bragg is being imaged, but there is a depolarized term contributing also to the backscattering. An increase in β_1 is related to higher surface roughness producing depolarization and an increase in the entropy. To complement the polarimetric study and gain additional insights into the nonpolarized contribution of the sea backscattering, the PR for the available quad-pol data takes is represented as a function of the incidence angle in Fig. 10. The PR p_B for the pure Bragg model is also included as solid black line.

Before NF [see Fig. 10(a)], an important difference between the estimated PR and p_B exists, which means that an important contribution on nonpolarized returns is presented, probably related to breaking wave effects. Even for the high incidence region (above 36°), where Bragg scattering is expected to be dominant, as stated in [10], an appreciable divergence between the PRs is observed (e.g., TSX-15 and TSX-17). Nevertheless, as pointed out throughout this paper, the reduced SNR conditions (≈3–4 dB) can explain this effect, since the thermal noise is also a nonpolarized component common to both copolar channels. This can be recognized from Fig. 10(b), where the difference between PR and p_B has been reduced for the high incidence angle region after NF.[9]

Following the two-component NRCS model (Bragg/non-Bragg) proposed by Kudryavtsev *et al.* [15], the relative

[9]In Fig. 10, the images have been radiometrically calibrated before the application of any further processing, i.e., the NESZ has been subtracted (in linear units) from the calibrated digital pixels, as proposed in [18]. From these results, it can be seen that there is still some residual noise that should be filtered out and that quad-pol data provide the means to do so.

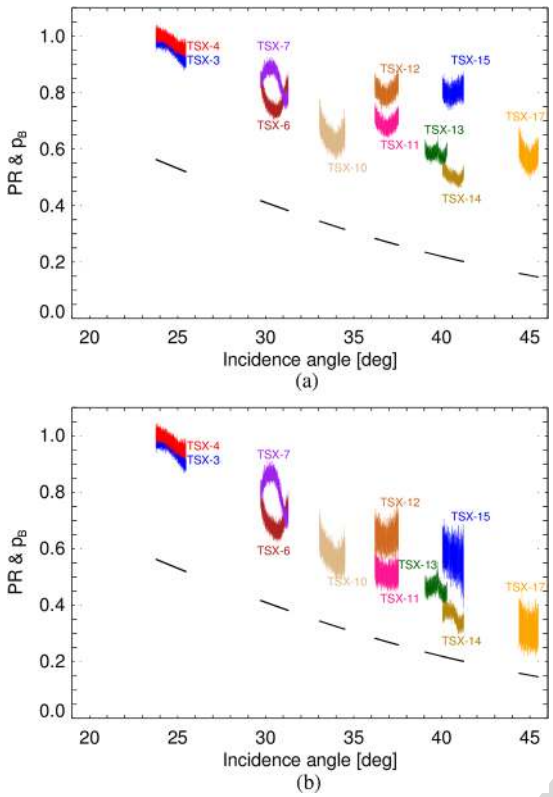

Fig. 10. PR as a function of the incidence angle for the different quad-pol data takes (color-coded as in Fig. 2): (a) before and (b) after NF; solid black lines refer to the PR for pure Bragg p_B.

TABLE IV
β_1 (ROUGHNESS) PROVIDING THE MINIMUM AVERAGE ERROR BETWEEN ESTIMATED PR FROM X/X2-BRAGG DATA FITTING AND MEASURED PR FOR QUAD-POL ACQUISITIONS AFTER NF

ID	X-Bragg	X2-Bragg
TSX-3	84	83.3
TSX-4	87	87
TSX-6	59	56
TSX-7	73	72
TSX-10	51	46.7
TSX-11	51	46.7
TSX-12	63	62
TSX-13	50	44.7
TSX-14	41	32.7
TSX-15	62	60.7
TSX-17	43	34.3

contribution of the non-Bragg component with respect to the total backscattered power for the S_{HH} channel ($\sigma^{0nB}/\sigma^0_{\mathrm{HH}}$) has been computed, and it ranges from 50% to 90% (high to small incidence angles), whereas for VV, the figures ($\sigma^{0nB}/\sigma^0_{\mathrm{VV}}$) are around 20%–70%. These results are in line with the studies carried out in [15] and [29]. For TSX-3 and TSX-4, $\sigma^{0nB}/\sigma^0_{\mathrm{VV}}$ and $\sigma^{0nB}/\sigma^0_{\mathrm{HH}}$ have very similar trends close to the 90% of the total backscattered power. In this very case, with the smallest incidence angle (25°), specular returns may partially contribute to the non-Bragg scattering [10], apart from possible breaking wave effects.

A fitting of the X-Bragg and X2-Bragg models to the measured PR has been carried out. After NF, β_1 values providing the minimum average error (between the models and the data) within each quad-pol acquisition are summarized in Table IV. As described in Section VI-B, an increase in β_1 is related to a roughness enhancement and thus a higher depolarization contribution. From Table IV, it can be generally stated that β_1 reduces as a function of the incidence angle in accordance to the decrease of the nonpolarized component. For the X2-Bragg model, β_1 corresponds to the average value for three different temporal decorrelation conditions assumed in the model ($\rho_{\mathrm{temp}} = 1.0, 0.95, 0.90$). Due to the presence of thermal noise and possible temporal decorrelations, the X-Bragg model overestimates the surface roughness, when compared with the proposed X2-Bragg model, particularly for the high incidence region (above 36°).

VII. CONCLUSION

A signal-based characterization of the sea/ocean returns imaged by TSX sensor has been carried out exploiting 17 data sets, both dual- and quad-pol. The transversal study copes with radiometric, statistical, and polarimetric analysis of the experimental data. One of the goals of this paper is to provide additional insights into proper modeling and characterization of the sea clutter response when observed by TSX.

First, the different results indicate that, for the quad-polarized data over maritime scenarios, the thermal noise impact can be a limiting factor in the correct interpretation of the TSX data, particularly for the low sea backscattering regions (incidence angles above 36°). Second, taking into account the specific DRA configuration to acquire quad-pol data, the induced temporal decorrelation of the sea returns between the polarimetric channels (due to the along-track configuration) is an additional limiting factor that should be carefully considered. This effect, combined with the additional thermal decorrelation, needs to be properly accounted for when trying to fit polarimetric physical-based models to the experimental data, in order to avoid misinterpretation. In this line, this paper proposes a new modeling approach to include such system/scenario dependent limitations applied specifically to the X-Bragg model and concreted in the new X2-Bragg model.

The NRCS analysis shows that the semiempirical model XMOD2 provides a fair fitting to the measured σ^0. Nevertheless, further studies are required to obtain a refined tunning of the XMOD2 coefficients from quad-pol TSX data sets for a wide range of sea conditions, ensuring that adequate calibration of the DRA mode can be accomplished.

Deviation from the Gaussian statistics for the TSX sea data is observed, when sufficient SNR is available and for small to medium incidence angles (below 36°). This means spikier returns and thus heavy-tailed amplitude distributions. The log-cumulant analysis shows that, for TSX, the ocean has high texture due to the higher resolution of the sensor coupled with the higher operating frequency (higher sensitivity to surface roughness variation). These results are in line with the study of the PR, which indicates an important contribution of non-Bragg scattering (depolarization), particularly for small incidence angles. As indicated in [15], [28], and [29], the presence of breaking wave events, increasing surface roughness and producing spikier returns, can explain this high depolarized

contribution. These nonpolarized returns tend to reduce as the incidence angle increases.

Exploiting the fully polarimetric information through the $H/\overline{\alpha}$ plane indicates that, for small incidence angles, the dominant scattering mechanism corresponds to low to medium random surface. The proposed X2-Bragg model proves a quite good fitting to the data in the $H/\overline{\alpha}$ plane. Therefore, the type of average mechanism and the relative strength between the involved scattering mechanisms can be well described by this model. In fact, since the X2-Bragg model, like the original X-Bragg, accounts for depolarization in the surface scattering, it is able to properly describe the presence of nonpolarized returns through the β_1 parameter (roughness measure). The fitting of the X2-Bragg to the measured PR indicates that there exists an important contribution of nonpolarized mechanisms (β_1 values are different from zero, i.e., pure Bragg). Comparatively, the X-Bragg model tends to produce an overestimation of the roughness (β_1) mainly due to the noise contribution. It has been also recognized that the fully polarimetric data can be exploited to apply an additive NF; otherwise, an overestimation of the PR and thus the roughness for both models is expected.

In summary, the study here presented shows that experimental quad-pol TSX acquisitions over the ocean have intrinsic system/scenario limitations (noise and temporal decorrelation), which should be carefully analyzed to avoid an erroneous interpretation of the polarimetric data. This paper sets the theoretical and analytical foundations to extrapolate the inclusion of such impacts to other physical-based scattering models, evaluating their effectiveness with experimental quad-pol data from current state-of-the-art polarimetric SAR sensors.

APPENDIX A
X2-BRAGG DERIVATION

In the following lines, an extension of the X-Bragg model, referred as X2-Bragg, is presented to introduce the impact of both noise and additional temporal decorrelations, in a two-step procedure.

First of all, let us define an equivalent coherency matrix, which accounts for the noise perturbation as (analogous to the study in [19])

$$\mathbf{T}' = \mathbf{T} + \mathbf{N} \tag{8}$$

where $\mathbf{T}$ refers to the expected coherency matrix related to the sea clutter, and the noise coherency matrix is diagonal $\mathbf{N} = \sigma_n^2 \mathbf{I}_{3\times 3}$. For simplicity, it has been assumed that the different polarimetric channels have uncorrelated additive circular complex Gaussian noise with the same power σ_n^2.

From the previous considerations, and using a general formulation, (8) can be expressed as

$$\mathbf{T}' = \left(\sigma_1^2 + \sigma_n^2\right) \overline{\mathbf{T}}' \tag{9}$$

where the normalized (to $\mathbf{T}'_{11}$) coherency matrix $\overline{\mathbf{T}}'$ is written as

$$\overline{\mathbf{T}}' = \begin{bmatrix} 1 & \sqrt{\frac{\sigma_2^2}{\sigma_1^2}} \overbrace{\rho_{\mathrm{SNR}_1}\rho_{12}}^{\rho_T} & 0 \\ \sqrt{\frac{\sigma_2^2}{\sigma_1^2}}\rho_{\mathrm{SNR}_1}\rho_{12}^* & \frac{\sigma_2^2}{\sigma_1^2}\frac{1+1/\mathrm{SNR}_2}{1+1/\mathrm{SNR}_1} & 0 \\ 0 & 0 & \frac{\sigma_3^2}{\sigma_1^2}\frac{1+1/\mathrm{SNR}_3}{1+1/\mathrm{SNR}_1} \end{bmatrix} \tag{10}$$

where σ_1^2, σ_2^2, and σ_3^2 refer to the signal power of the three polarimetric channels (in the Pauli base); SNR_1, SNR_2, and SNR_3 are the corresponding SNRs, i.e., $\mathrm{SNR}_i = \sigma_i^2/\sigma_n^2$; ρ_{12} represents the polarimetric correlation (coherence) coefficient between $(S_{\mathrm{HH}} + S_{\mathrm{VV}})$ and $(S_{\mathrm{HH}} - S_{\mathrm{VV}})$ channels; and ρ_{SNR_1} models the decorrelation effect induced by the presence of thermal noise, i.e.,

$$\rho_{\mathrm{SNR}_1} = \frac{1}{1 + 1/\mathrm{SNR}_1} \tag{11}$$

such that the total coherence, based on a multiplicative model, is defined as ρ_T.

From the original X-Bragg model formulation in (7), the different parameters in (10) can be expressed as

$$\begin{aligned} \sigma_1^2 &= m_s^2 C_1 \\ \sigma_2^2 &= m_s^2 C_3 \left(1 + \mathrm{sinc}(4\beta_1)\right) \\ \sigma_3^2 &= m_s^2 C_3 \left(1 - \mathrm{sinc}(4\beta_1)\right) \\ \rho_{12} &= \frac{C_2 \mathrm{sinc}(2\beta_1)}{\sqrt{C_1 C_3 \left(1 + \mathrm{sinc}(4\beta_1)\right)}}. \end{aligned} \tag{12}$$

From the previous relationships, the three polarimetric SNRs can be defined in terms of an equivalent $\mathrm{SNR}_{\mathrm{Eq}}$ as

$$\begin{aligned} \mathrm{SNR}_1 &= C_1 \mathrm{SNR}_{\mathrm{Eq}} \\ \mathrm{SNR}_2 &= C_3 \left(1 + \mathrm{sinc}(4\beta_1)\right) \mathrm{SNR}_{\mathrm{Eq}} \\ \mathrm{SNR}_3 &= C_3 \left(1 - \mathrm{sinc}(4\beta_1)\right) \mathrm{SNR}_{\mathrm{Eq}} \end{aligned} \tag{13}$$

in a way that, if SNR_1 is estimated from the data, the equivalent $\mathrm{SNR}_{\mathrm{Eq}} = m_s^2/\sigma_n^2$ can be inverted from the model and used to properly account for the thermal noise impact in the X-Bragg model fitting.

In multichannel adaptive array and GMTI theory, the impact of temporal decorrelation is known to cause an increase in the number of eigenvalues (of the clutter-plus-noise covariance matrix) different from the noise floor [3]. The X-Bragg model has been further extended to account for temporal decorrelation, in terms of an additional coherence coefficient ρ_{temp}. It must be noted that this term cannot be directly introduced in matrix (10) since, from the DRA acquisition itself, the temporal decorrelation is between the individual polarimetric channels with some spatial or temporal baseline. This additional term should be considered in the covariance matrix $\mathbf{C}$ formulation. First, a transformation of the normalized coherency matrix $\overline{\mathbf{T}}'$ (10) into the covariance matrix is performed as

$$\overline{\mathbf{C}}' = \left\{\mathbf{U}_{3(\mathrm{L}\to\mathrm{P})}\right\}^{-1} \overline{\mathbf{T}}' \left\{\mathbf{U}_{3(\mathrm{L}\to\mathrm{P})}^H\right\}^{-1} \tag{14}$$

where the unitary transformation $(\mathrm{L} \to \mathrm{P})$ from the lexicographic target vector to the Pauli vector is

$$\mathbf{U}_{3(\mathrm{L}\to\mathrm{P})} = \frac{1}{\sqrt{2}} \begin{bmatrix} 1 & 0 & 1 \\ 1 & 0 & -1 \\ 0 & \sqrt{2} & 0 \end{bmatrix}. \tag{15}$$

Then, the additional coherence coefficient ρ_{temp} is included as multiplicative term into the off-diagonal terms of $\overline{\mathbf{C}}'$ to obtain $\overline{\mathbf{C}}''$. The normalized coherency matrix for the X2-Bragg model

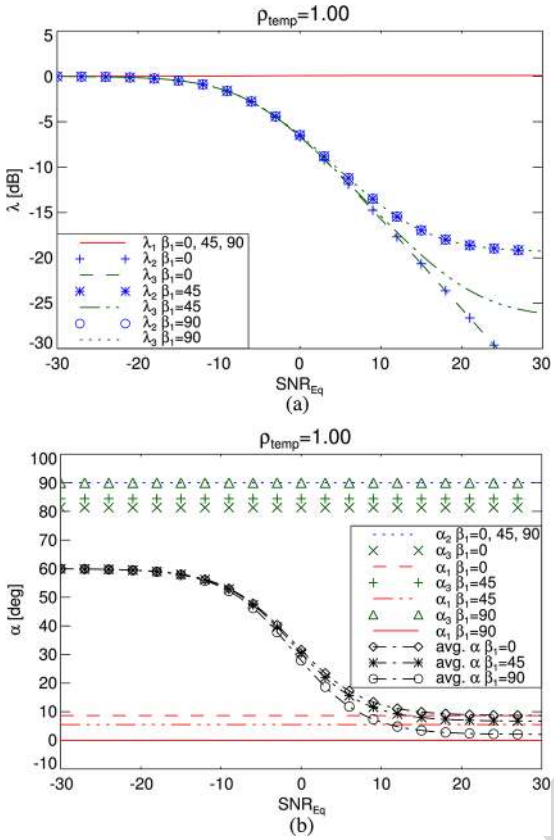

Fig. 11. Sensitivity w.r.t. $\mathrm{SNR}_{\mathrm{Eq}}$ for the X2-Bragg model considering the noise impact and a temporal decorrelation $\rho_{\mathrm{temp}} = 1.0$ for three values of the uniform distribution width β_1; an X-band system (9.65 GHz), an incidence angle $\gamma = 24.6°$, a sea temperature of 10 °C, and salinity of 35‰ are considered. (a) Eigenvalues. (b) Alphas.

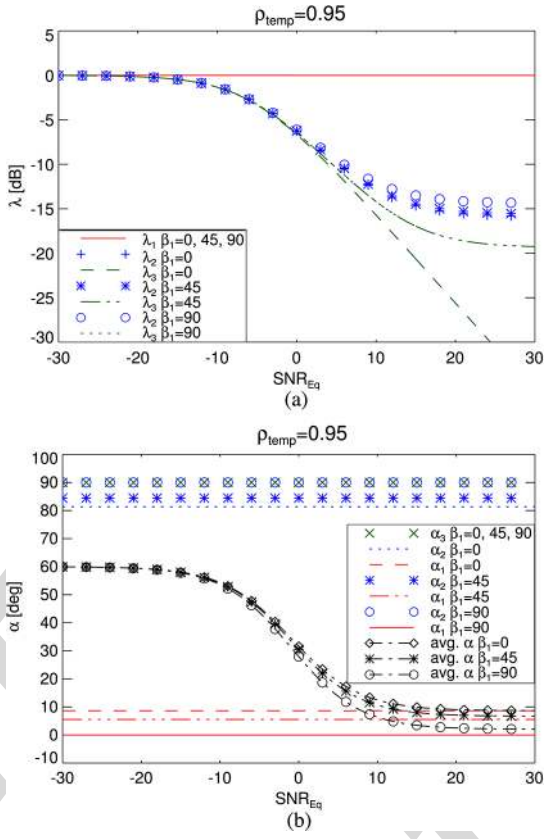

Fig. 12. Sensitivity w.r.t. $\mathrm{SNR}_{\mathrm{Eq}}$ for the X2-Bragg model considering the noise impact and a temporal decorrelation $\rho_{\mathrm{temp}} = 0.95$ for three values of the uniform distribution width β_1; an X-band system (9.65 GHz), an incidence angle $\gamma = 24.6°$, a sea temperature of 10 °C, and salinity of 35‰ are considered. (a) Eigenvalues. (b) Alphas.

$\overline{\mathbf{T}}''$ can be obtained using a matrix transformation of $\overline{\mathbf{C}}''$ by means of $\mathbf{U}_{3(\mathrm{L}\to\mathrm{P})}$, inversely analogous to the case in (14).

APPENDIX B
X2-BRAGG THEORETICAL EVALUATION

The sensitivity of the eigenvalues and α parameters as a function of $\mathrm{SNR}_{\mathrm{Eq}}$ for $\rho_{\mathrm{temp}} = 1.0$ and $\rho_{\mathrm{temp}} = 0.95$ is shown, respectively, in Figs. 11 and 12, exploiting the theoretical coherency matrix formulation $\overline{\mathbf{T}}''$ of the X2-Bragg model. It has been assumed an X-band system (9.65 GHz), an incidence angle γ of 24.6° [corresponding to the center of TSX-4 acquisition (see Table I)], and sea conditions of 10 °C and 35‰ salinity content. In Figs. 11(a) and 12(a), the eigenvalue distribution is represented as a function of $\mathrm{SNR}_{\mathrm{Eq}}$. The three eigenvalues collapse, regardless of β_1 and ρ_{temp}, when reducing $\mathrm{SNR}_{\mathrm{Eq}}$ (< -10 dB), being the noise the dominant mechanism.

In case of $\beta_1 = 0°$ (smooth surface) and with increasing $\mathrm{SNR}_{\mathrm{Eq}}$, the two smallest eigenvalues λ_2 (plus symbols) and λ_3 (dashed line) have the same decreasing trend when no temporal decorrelation is included [see Fig. 11(a)]. Their contribution is 30 dB below λ_1 for $\mathrm{SNR}_{\mathrm{Eq}} > 20$ dB, in which case SPM applies with a single dominant mechanism. This can be observed also from the averaged value $\overline{\alpha}$ [dash–dot line with diamond markers in Fig. 11(b)], which tends to α_1 (dashed line). As β_1 (roughness) increases, the cross-polar power increases; hence, more than a single dominant mechanism exist. For $\beta_1 = 45°$ and $\mathrm{SNR}_{\mathrm{Eq}} > 10$ dB, the two smallest eigenvalues (asterisk symbols and dash–dot–dot line) start to diverge. In the limit $\beta_1 = 90°$ and with no additional temporal decorrelation, λ_2 (circle markers) and λ_3 (dotted line) have the same trend as a function of the effective SNR, since polarimetric coherence ρ_{12} decreases to 0. Considering a temporal decorrelation of the sea $\rho_{\mathrm{temp}} = 0.95$, a general increase of the second eigenvalue can be recognized (for $\mathrm{SNR}_{\mathrm{Eq}} > 10$ dB), comparing Figs. 11(a) and 12(a), particularly for $\beta_1 = 0°$. In case of λ_3, this behavior is also observed, but for $\beta_1 \geq 45°$.

Contrary to the eigenvalues, the individual α parameters are almost unaffected by the presence of noise, as shown in Figs. 11(b) and 12(b). Polarimetric decomposition considers the mean $\overline{\alpha}$, based on proper weighting of the individual α terms through the eigenvalues' probabilities [14]. As shown in Figs. 11(b) and 12(b), the average $\overline{\alpha}$ presents a large variation as a function of $\mathrm{SNR}_{\mathrm{Eq}}$ for different values of β_1. In the limit, $\overline{\alpha}$ tends to 60°, such that the scattering mechanism lies in the extreme edge of region 2 of the Cloude–Pottier $H/\overline{\alpha}$, i.e., random noise, that is, no polarization dependence. Temporal decorrelation exchanges the behavior of the individual α_2 and α_3 parameters, comparing Figs. 11(b) and 12(b), but does not affect the averaged values: when no temporal decorrelation

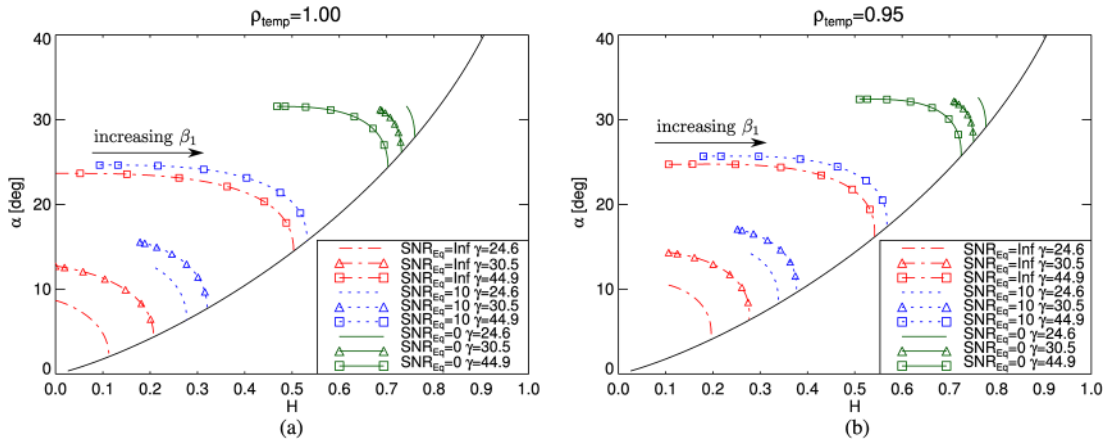

Fig. 13. $H/\overline{\alpha}$ plane for the X2-Bragg model at three incidence angles (24.6°, 33.8°, and 44.9°) and for three $\mathrm{SNR_{Eq}}$ conditions (∞, 10 dB, and 0 dB): (a) $\rho_{\mathrm{temp}} = 1.0$ and (b) $\rho_{\mathrm{temp}} = 0.95$ (sea water with salinity content of 35‰ and temperature of 10 °C).

is considered ($\rho_{\mathrm{temp}} = 1$), α_2 collapses to 90° regardless of β_1, and α_3 sweeps the values from 80° to 90°, whereas for $\rho_{\mathrm{temp}} = 0.95$, α_3 is 90° for the different roughness parameters. Therefore, temporal decorrelation is not impairing the values of α parameters, but it is modulating the contribution of the different mechanisms, i.e., for $\rho_{\mathrm{temp}} = 0.95$, the cross-polar component (related to $\alpha = 90$ independently from β_1) is no longer the second dominant scattering mechanism (as for $\rho_{\mathrm{temp}} = 1$).

The impact of both thermal noise and temporal decorrelation in the X2-Bragg model is also analyzed in the $H/\overline{\alpha}$ plane, as represented in Fig. 13(a) and (b) for $\rho_{\mathrm{temp}} = 1$ and $\rho_{\mathrm{temp}} = 0.95$, respectively. Different incidence angles, corresponding to the center of data takes TSX-4 (24.6°), TSX-7 (30.5°), and TSX-17 (44.9°), are considered. The noise impact is translated into a progressive increase of both $\overline{\alpha}$ and H as $\mathrm{SNR_{Eq}}$ decreases. Moreover, the variation of the $H/\overline{\alpha}$ pairs as a function of β_1 is reduced when the noise contribution increases. Temporal decorrelation produces similar effects, but its impact reduces as long as the entropy increases, clearly visible for the region with $H > 0.6$ when comparing Fig. 13(a) and (b).

A particular case in the $H/\overline{\alpha}$ plane is recognized for $\mathrm{SNR_{Eq}} = 0$ dB, where the variation as a function of the incidence angle is reversed, i.e., the near range presents higher entropy values than the far range: as long as the noise contribution increases, the divergence between the two smallest eigenvalues (λ_2 and λ_3) reduces (increasing the entropy), and this effect is more severe for the near range. This relative separation is also a function of the roughness (β_1), which, for noisy near range scenarios, is quite flat. Such a response justifies the reduction on H as a function of β_1 for increasing noise, particularly at near range.

ACKNOWLEDGMENT

The authors would like to thank the German Aerospace Center (DLR) and, in particular, S. Baumgartner for the TSX quad-pol data provided in the frame of the DRA proposal MTH1971 and the FP7-SPACE Project NEREIDS Ref. 263468 for the TSX dual-pol data. The authors would also like to thank A. Gómez for her helpful suggestions and comments.

REFERENCES

[1] S. Hasselmann, C. Brüning, K. Hasselmann, and P. Heimbach, "An improved algorithm for the retrieval of ocean wave spectra from synthetic aperture radar image spectra," *J. Geophys. Res., Oceans*, vol. 101, no. C7, pp. 16 615–16 629, Jul. 1996.

[2] R. Goldstein and H. Zebker, "Interferometric radar measurement of ocean surface currents," *Nature*, vol. 328, no. 6132, pp. 707–709, Aug. 1987.

[3] E. Makhoul, A. Broquetas, J. Ruiz-Rodon, Y. Zhan, and F. Ceba, "A performance evaluation of SAR-GMTI missions for maritime applications," *IEEE Trans. Geosci. Remote Sens.*, vol. 53, no. 5, pp. 2496–2509, May 2015.

[4] M. Gabele *et al.*, "Fore and aft channel reconstruction in the TerraSAR-X dual receive antenna mode," *IEEE Trans. Geosci. Remote Sens.*, vol. 48, no. 2, pp. 795–806, Feb. 2010.

[5] I. Hajnsek, E. Pottier, and S. Cloude, "Inversion of surface parameters from polarimetric SAR," *IEEE Trans. Geosci. Remote Sens.*, vol. 41, no. 4, pp. 727–744, Apr. 2003.

[6] X.-M. Li and S. Lehner, "Algorithm for sea surface wind retrieval from TerraSAR-X and TanDEM-X data," *IEEE Trans. Geosci. Remote Sens.*, vol. 52, no. 5, pp. 2928–2939, May 2014.

[7] T. Fritz and M. Eineder, "TerraSAR-X: Ground segment basic product specification document," German Aerosp. Center (DLR), Köln, Germany, Tech. Rep. TX-GS-DD-3302, Oct. 2013.

[8] K. D. Ward, R. J. Tough, and S. Watts, *Sea Clutter: Scattering, the K Distribution and Radar Performance*. Stevenage, U.K.: The Insti. Eng. Technol., 2006.

[9] S. Anfinsen and T. Eltoft, "Application of the matrix-variate Mellin transform to analysis of polarimetric radar images," *IEEE Trans. Geosci. Remote Sens.*, vol. 49, no. 6, pp. 2281–2295, Jun. 2011.

[10] S. Skrunes, C. Brekke, T. Eltoft, and V. Kudryavtsev, "Comparing near-coincident C- and X-band SAR acquisitions of marine oil spills," *IEEE Trans. Geosci. Remote Sens.*, vol. 53, no. 4, pp. 1958–1975, Apr. 2015.

[11] E. Jakeman and P. N. Pusey, "A model for non-Rayleigh sea echo," *IEEE Trans. Antennas Propag.*, vol. AP-24, no. 6, pp. 806–814, Nov. 1976.

[12] K. Ouchi and R. Cordey, "Statistical analysis of azimuth streaks observed in digitally processed CASSIE imagery of the sea surface," *IEEE Trans. Geosci. Remote Sens.*, vol. 29, no. 5, pp. 727–735, Sep. 1991.

[13] D. Trizna, "Statistics of low grazing angle radar sea scatter for moderate and fully developed ocean waves," *IEEE Trans. Antennas Propag.*, vol. 39, no. 12, pp. 1681–1690, Dec. 1991.

[14] S. Cloude and E. Pottier, "An entropy based classification scheme for land applications of polarimetric SAR," *IEEE Trans. Geosci. Remote Sens.*, vol. 35, no. 1, pp. 68–78, Jan. 1997.

[15] V. Kudryavtsev, D. Hauser, G. Caudal, and B. Chapron, "A semiempirical model of the normalized radar cross-section of the sea surface 1. Background model," *J. Geophys. Res., Oceans*, vol. 108, no. C3, pp. FET 2-1–FET 2-24, Mar. 2003.

[16] J. Morris, S. Anderson, and S. Cloude, "A study of the X-band entropy of breaking ocean waves," in *Proc. IEEE IGARSS*, Jul. 2003, vol. 2, pp. 711–713.

[17] D. A. Gagliardini and P. C. Colón, "Ocean feature detection using microwave backscatter and sun glint observations," *Gayana (Concepción)*, vol. 68, no. 2, pp. 180–185, 2004.

[18] AIRBUS, "Radiometric calibration of TerraSAR-X data: Beta naught and sigma naught coefficient calculation," AIRBUS Defence Space, Munich, Germany, Tech. Rep. TSXX-ITD-TN-0049, Mar. 2014.
[19] C. López-Martínez, A. Alonso-González, and X. Fabregas, "Perturbation analysis of eigenvector-based target decomposition theorems in radar polarimetry," *IEEE Trans. Geosci. Remote Sens.*, vol. 52, no. 4, pp. 2081–2095, Apr. 2014.
[20] V. Gregers-Hansen and R. Mital, "An improved empirical model for radar sea clutter reflectivity," *IEEE Trans. Aerosp. Electron. Syst.*, vol. 48, no. 4, pp. 3512–3524, Oct. 2012.
[21] F. E. Nathanson, J. P. Reilly, and M. N. Cohen, *Radar Design Principles: Signal Processing and the Environment*, 2nd ed. New York, NY, USA: McGraw-Hill, 1990.
[22] M. Menon, "Estimation of the shape and scale parameters of the Weibull distribution," *Technometrics*, vol. 5, no. 2, pp. 175–182, May 1963.
[23] D. Iskander and A. Zoubir, "Estimation of the parameters of the K-distribution using higher order and fractional moments [radar clutter]," *IEEE Trans. Aerosp. Electron. Syst.*, vol. 35, no. 4, pp. 1453–1457, Oct. 1999.
[24] D. Blacknell and R. J. A. Tough, "Parameter estimation for the K-distribution based on [z log(z)]," *Proc. Inst. Elect. Eng.—Radar Sonar Navig.*, vol. 148, no. 6, pp. 309–312, Dec. 2001.
[25] R. J. A. Tough, D. Blacknell, and S. Quegan, "A statistical description of polarimetric and interferometric synthetic aperture radar data," *Proc. R. Soc. Lond. A, Math. Phys. Sci.*, vol. 449, no. 1937, pp. 567–589, Jun. 1995.
[26] D. Schuler and J. Lee, "Mapping ocean surface features using biogenic slick-fields and SAR polarimetric decomposition techniques," *Proc. Inst. Elect. Eng.—Radar Sonar Navig.*, vol. 153, no. 3, pp. 260–270, Jun. 2006.
[27] M. Migliaccio, A. Gambardella, and M. Tranfaglia, "SAR polarimetry to observe oil spills," *IEEE Trans. Geosci. Remote Sens.*, vol. 45, no. 2, pp. 506–511, Feb. 2007.
[28] A. Voronovich and V. Zavorotny, "Theoretical model for scattering of radar signals in Ku-and C-bands from a rough sea surface with breaking waves," *Waves Random Media*, vol. 11, no. 3, pp. 247–269, 2001.
[29] A. A. Mouche, D. Hauser, and V. Kudryavtsev, "Radar scattering of the ocean surface and sea-roughness properties: A combined analysis from dual-polarizations airborne radar observations and models in C band," *J. Geophys. Res., Oceans*, vol. 111, no. C9, Sep. 2006, Art. ID. C09004.
[30] D. Schuler, J.-S. Lee, and K. Hoppel, "Polarimetric SAR image signatures of the ocean and gulf stream features," *IEEE Trans. Geosci. Remote Sens.*, vol. 31, no. 6, pp. 1210–1221, Nov. 1993.
[31] L. Klein and C. Swift, "An improved model for the dielectric constant of sea water at microwave frequencies," *IEEE Trans. Antennas Propag.*, vol. AP-25, no. 1, pp. 104–111, Jan. 1977.
[32] R. Romeiser and D. Thompson, "Numerical study on the along-track interferometric radar imaging mechanism of oceanic surface currents," *IEEE Trans. Geosci. Remote Sens.*, vol. 38, no. 1, pp. 446–458, Jan. 2000.

Eduardo Makhoul (S'09–M'15) was born in Homs, Siria, in 1985. He received the M.Sc. degree in electrical engineering and the Ph.D. degree (*cum laude*) from Universitat Politècnica de Catalunya (UPC), Barcelona, Spain, in 2009 and 2015, respectively.

In 2008, he worked on his master thesis in the frame of high-resolution wide-swath synthetic aperture radar (SAR) systems at the German Aerospace Center (DLR). In 2009, he joined the Remote Sensing Laboratory, UPC, researching on aspects of ground moving target indication (GMTI) for future spaceborne SAR systems. From 2009 to 2011, he worked on the radiometric budget analysis of the Spanish mission PAZ. From 2010 to 2013, he worked on the analysis and study of SAR-GMTI systems and techniques for future European missions in the frame of NEWA and SIMTISYS projects. In 2013 (April–August), he was a Visiting Researcher with DLR, working on SAR-GMTI processing of airborne and spaceborne data over maritime scenarios. Since August 2015, he has been with IsardSAT, an experienced Earth observation research company in Barcelona, involved in the design, calibration, and maintenance of civil remote sensing instruments. His main research interests include SAR, GMTI, radar system design, mission performance, calibration, array signal processing, sea/ocean surveillance, and polarimetry.

Carlos López-Martínez (S'97–M'04–SM'11) received the M.Sc. degree in electrical engineering and the Ph.D. degree from Universitat Politècnica de Catalunya (UPC), Barcelona, Spain, in 1999 and 2003, respectively.

From October 2000 to March 2002, he was with the Frequency and Radar Systems Department, HR, German Aerospace Center (DLR), Oberpfaffenhofen, Germany. From June 2003 to December 2005, he was with the Image and Remote Sensing Group SAPHIR Team of the Institute of Electronics and Telecommunications of Rennes (IETR CNRS UMR 6164), Rennes, France. In January 2006, he joined UPC, Barcelona, as a Ramón y Cajal Researcher. He is currently an Associate Professor in the area of remote sensing and microwave technology with UPC. He has authored or coauthored over 100 articles in journals, books, and conference proceedings in the radar remote sensing and image analysis literature. His research interests include SAR and multidimensional SAR, radar polarimetry, physical parameter inversion, digital signal processing, estimation theory, and harmonic analysis.

Dr. López-Martínez is an Associate Editor of the IEEE JOURNAL OF SELECTED TOPICS IN APPLIED EARTH OBSERVATIONS AND REMOTE SENSING. He served as a Guest Editor of the *EURASIP Journal on Advances in Signal Processing*. He has organized different invited sessions in international conferences on radar and SAR polarimetry. He has presented advanced courses and seminars on radar polarimetry to a wide range of organizations and events. He was a recipient of the Student Prize Paper Award at the EUSAR 2002 Conference and coauthored the paper awarded with the First Place Student Paper Award at the EUSAR 2012 Conference. He has been also a recipient of the IEEE Geoscience and Remote Sensing Society 2013 GOLD Early Career Award.

Antoni Broquetas (S'84–M'90) was born in Barcelona, Spain, in 1959. He received the Ingeniero degree in telecommunications engineering and the Doctor Ingeniero degree in telecommunications engineering (for his work on microwave tomography) from Universitat Politècnica de Catalunya (UPC), Barcelona, in 1985 and 1989, respectively.

In 1986, he was a Research Assistant with Portsmouth Polytechnic, Portsmouth, U.K., involved in propagation studies. In 1987, he joined the Department of Signal Theory and Communications (TSC), UPC, where he was the Subdirector of Research of the Institute of Geomatics from 1998 to 2002 and the Director of TSC from 2003 to 2006. Since 1999, he has been a Full Professor with UPC, involved in research on radar imaging and remote sensing. He has authored or coauthored over 150 papers on microwave tomography, radar, ISAR and SAR systems, and SAR processing and interferometry.

AUTHOR QUERIES

AUTHOR PLEASE ANSWER ALL QUERIES

Please be aware that authors are required to pay overlength page charges ($200 per page) if the paper is longer than 6 pages. If you cannot pay any or all of these charges please let us know.

This pdf contains 2 proofs. The first half is the version that will appear on Xplore. The second half is the version that will appear in print. If you have any figures to print in color, they will be in color in both proofs.

The "Open Access" option for your paper expires when the paper is published on Xplore in an issue with page numbers. Papers in "Early Access" may be changed to "Open Access."

AQ1 = Please check if changes made in the affiliation of author E. Makhoul are correct. Otherwise, please make the necessary changes.
AQ2 = Please provide the expanded form of "DFO."

END OF ALL QUERIES

Exploiting Polarimetric TerraSAR-X Data for Sea Clutter Characterization

Eduardo Makhoul, *Member, IEEE*, Carlos López-Martínez, *Senior Member, IEEE*, and Antoni Broquetas, *Member, IEEE*

***Abstract*—This paper presents a detailed characterization of sea/ocean clutter returns at X-band, imaged by TerraSAR-X (TSX) mission from the radiometric, statistical, and polarimetric standpoints. Different TSX data takes, covering the typical spaceborne incidence angle region (20°–45°), are analyzed: dual-polarized and experimental quad-polarized (quad-pol) data have been used. The thermal noise of the receiver for quad-pol data turns out to be an important limitation in the sea characterization from TSX, particularly at high incidence angles (above 36°), where low signal-to-noise ratios (SNRs) can impair the proper data distribution fitting and the polarimetric backscattering description. Statistical analysis shows large deviation from Gaussianity, indicating presence of texture, mainly in the small incidence region (20°–36°), with favorable SNR conditions. The different polarimetric features revealed contribution of nonpolarized scattering, related to the presence of breaking waves. This paper also proposes and evaluates an extension of the well-known X-Bragg model, named X2-Bragg (extended-extended Bragg), which properly accounts for the impact of thermal noise and sea clutter temporal decorrelation, due to the dual receive antenna acquisition mode. Such additional decorrelation sources, if not properly analyzed and accounted for in the physical-based model description, could lead to an incorrect interpretation of the polarimetric properties and the related erroneous geophysical parametric inversion from the real data. In this sense, the X2-Bragg proves its fitting to the experimental data, quantifying accordingly the presence of nonpolarized scattering in terms of the roughness parameter β_1.**

***Index Terms*—Non-Gaussian clutter, parameter estimation, radar backscattering coefficient, sea clutter, statistical analysis, synthetic aperture radar (SAR), SAR polarimetry, X-Bragg.**

I. Introduction

THE imaging capability of synthetic aperture radars (SARs), independent from daylight and weather conditions, represents a potential tool for globally monitoring the ocean. SAR is a very important forecast instrument in oceanography, allowing, among others, the retrieval of ocean wave spectrums [1] and the measurement of ocean or river current velocities [2]. Lately, the increase in vessel hijacking, as well as the need to control fishing and tanker polluting activities, demand remote sensing systems to properly monitor maritime traffic. SAR sensors with ground moving target indication (GMTI) capabilities are of great interest for ship surveillance [3].

Characterization and modeling of the sea clutter returns observed by SAR systems are of great interest for the accurate evaluation of future SAR missions imaging the sea. The availability of polarimetric SAR instruments, such as TerraSAR-X (TSX) or TanDEM-X (TDX), provides a unique opportunity to gather geophysical and biophysical information of the marine environment. This paper exploits different dual-pol (HH/HV[1]) and experimental quad-pol TSX data sets (covering 20°–45° of incidence angle) to perform a transversal (radiometric, statistical, and polarimetric) and compact study of the sea echo returns. To the authors' knowledge, such analysis has not been performed yet, exploiting the experimental quad-pol data from TSX.

The main stress of the study is to point out the different limitations that may be encountered when operating TSX, particularly in the quad-pol mode, where the dual receive antenna (DRA) mode is used [4], such that the antenna is split into two halves (receiving H and V simultaneously) and the transmit polarization is toggled in a pulse basis. On one hand, there is an increase of 3 dB in the noise equivalent sigma zero (NESZ) due to a reduced antenna effective area per channel, i.e., 3-dB loss in signal-to-noise ratio (SNR). On the other hand, a temporal lag exists between the different polarimetric channels, during which sea clutter decorrelates. The identification of such technological-driven aspects from the signal-based analysis proves to be of key importance in the correct interpretation of the polarimetric data when fitting physical-based models. In this sense, the X-Bragg model [5], which extends the Bragg surface scattering to include the impact of depolarized and cross-polarized returns, has been optimized to account for such additional perturbations (noise+sea temporal decorrelations), based on a comprehensive theoretical formulation, leading to the extended-extended Bragg (X2-Bragg) model; otherwise, these additional decorrelation sources could produce an erroneous interpretation of the polarimetric backscattering properties when trying to fit the physical-based X-Bragg model to the experimental data.

The radiometric analysis, in terms of the radar backscattering coefficient σ^0, shows that, in TSX, the thermal noise of the re-

Manuscript received April 24, 2015; revised July 9, 2015; accepted July 12, 2015. This work was supported in part by the FPU Research Fellowship Program, Ministerio de Educación under Contract AP2009-4590; by the FI-AGAUR Research Fellowship Program, Generalitat de Catalunya under Contract 2010FI EM051757; and by the Spanish Ministry of Science and Innovation (MICINN) under projects TEC2011-28201-C02-01 and TIN2014-55413-C2-1-P.

E. Makhoul was with the Department of Signal Theory and Communications, Universitat Politècnica de Catalunya, 08034 Barcelona, Spain. He is now with isardSAT, 08042 Barcelona, Spain (e-mail: edumak@tsc.upc.edu).

C. López-Martínez and A. Broquetas are with the Department of Signal Theory and Communications, Universitat Politècnica de Catalunya, 08034 Barcelona, Spain (e-mail: carlos.lopez@tsc.upc.edu; broquetas@tsc.upc.edu).

Color versions of one or more of the figures in this paper are available online at http://ieeexplore.ieee.org.

Digital Object Identifier 10.1109/TGRS.2015.2457242

[1]H and V refer to horizontal and vertical polarizations, respectively.

TABLE I
TSX DATA TAKES USED IN THE SEA CLUTTER CHARACTERIZATION (BW_R AND BW_A ARE RANGE AND AZIMUTH PROCESSED BANDWIDTHS, v_{win} AND θ_{win} ARE WIND SPEED AND DIRECTION FROM WHICH THE WIND IS BLOWING)

ID	Date	Region	Location	Mode	γ [deg]	BW_R [MHz]	BW_A [Hz]	v_{win} [m/s]	θ_{win} [deg]
TSX-1	05.03.2013	Senegal	N15.07-W17.60	Duad-Pol	19.85-21.74	150	1380	-	-
TSX-2	09.03.2013	Gulf of Guinea	N3.56-W2.35	Duad-Pol	22.43-24.26	150	1380	-	-
TSX-3	25.04.2010	Vancouver Island	N49.72-W127.97	Quad-Pol	23.75-25.49	150	1380	12.1	143
TSX-4	06.05.2010	Vancouver Island	N49.72-W127.97	Quad-Pol	23.75-25.49	150	1380	6.3	331
TSX-5	16.03.2013	Mauritania	N19.45-W16.78	HH	24.80-27.99	150	2765	-	-
TSX-6	30.04.2010	Bermuda	N31.37-W69.54	Quad-Pol	29.70-31.30	150	1380	6.5	258
TSX-7	11.05.2010	Bermuda	N31.37-W69.54	Quad-Pol	29.70-31.30	150	1380	6.9	62
TSX-8	05.03.2013	Mauritania	N18.78-W17.43	Dual-Pol	30.81-32.33	150	1380	-	-
TSX-9	05.03.2013	Senegal	N13.91-W18.48	Dual-Pol	31.91-33.42	150	1380	-	-
TSX-10	12.04.2010	Barcelona	N41.23-E2.11	Quad-Pol	33.04-34.50	150	1380	-	-
TSX-11	28.04.2010	Southeast Yakutat	N58.20-W137.96	Quad-Pol	36.18-37.54	150	1380	7.2	164
TSX-12	09.05.2010	Southeast Yakutat	N58.20-W137.96	Quad-Pol	36.18-37.54	150	1380	5.7	350
TSX-13	23.04.2010	Pratas Island	N20.67-E116.92	Quad-Pol	39.03-40.29	150	1380	-	-
TSX-14	25.04.2010	South Hecate Strait	N52.37-W129.81	Quad-Pol	40.02-41.25	150	1380	13.1	140
TSX-15	06.05.2010	South Hecate Strait	N52.37-W129.81	Quad-Pol	40.02-41.25	150	1380	6.7	318
TSX-16	17.03.2013	Gulf of Guinea	N0.24-E7.97	Dual-Pol	43.45-44.58	150	1380	-	-
TSX-17	21.04.2010	North Sea	N54.38-E7.05	Quad-Pol	44.37-45.48	150	1380	-	-

ceiver could be an important limiting factor for proper sea clutter characterization (statistical and polarimetric backscattering fitting), particularly in the case of quad-polarized acquisitions and for the spaceborne high-incidence region (36°–45°) due to the reduced SNR conditions. The σ^0 model, i.e., XMOD2 [6], optimized from TSX/TDX dual-pol data, provides a close fitting to the measured data also for the quad-pol case, where remaining calibration issues on the experimental DRA mode may induce additional errors [7].

The statistical analysis based on the computation of the normalized intensity moments (NIM) [8], and complemented by the log-cumulants' study [9], [10] confirms deviation from Gaussian statistics for the high-resolution X-band system [8], [10]–[13], and mainly at incidence angles below 36°, where sufficient SNR is available.

To evaluate the scattering properties of the sea when imaged by TSX, the polarimetric roll-invariant parameters, i.e., entropy H and mean scattering angle $\overline{\alpha}$ described in [14], as well as the polarization ratio (PR) metrics [10], [15], have been exploited. The results indicate that most of the acquisitions lie in the low to medium random surface scattering region, mainly due to the important contribution of nonpolarized returns, as indicated by $H/\overline{\alpha}$ and PR analyses. The proposed X2-Bragg model shows a good fitting with the experimental data in the $H/\overline{\alpha}$ plane, providing a mechanism to model the nonpolarized returns in terms of β_1 parameter, which is an indicator of the surface roughness (breaking waves events are known to cause an increase in surface roughness [8], [16]).

The remainder of this paper is organized as follows. In Section II, the TSX data set is presented. The methodology followed to perform the sea clutter characterization is introduced in Section III. In Section IV, the radiometric analysis in terms of radar backscattering coefficient is presented. Later on, the statistical description of the experimental data set is analyzed in Section V. To end up the transversal characterization, a complete polarimetric analysis is carried out in Section VI. Conclusions are drawn in Section VII. A comprehensive derivation of the proposed X2-Bragg model and its theoretical evaluation are considered in Appendixes A and B.

II. DATA SET DESCRIPTION

The main parameters of the stripmap products used in the analysis are summarized in Table I. The different data sets are made up of acquisitions from both the TSX and TDX instruments. Different aspects were considered for the selection of the data under analysis: 1) covering the spaceborne SAR operational range of incidence angles from 20° to 45°; 2) avoiding heterogeneity in the reflectivity over the imaged area; 3) avoiding regions with high density of maritime traffic and/or marine littorals (because of the high ambiguities' impact in the DRA acquisition); and 4) when possible, polarimetric acquisition is preferred over single polarization.

The available fully polarimetric TSX data were acquired during the experimental DRA mode campaign, April and May 2010. It is well known that sea or ocean conditions, and hence their radar response, could be quite different depending on the geographical location of the marine scenario under analysis; this is why it has been tried to sample the acquisitions over different oceans (Atlantic and Pacific) and seas (North, Mediterranean, and China). For the nominal dual-polarization stripmap products, the absolute and relative radiometric accuracies are 0.6 and 0.3 dB, respectively; whereas for the quad-polarization products, there is no specification, since it is an experimental mode with few dedicated campaigns and additional investigations on the DRA calibration issues need to be considered [7].

Portions of the images of three representative data takes (near/TSX-4, middle/TSX-7, and far range/TSX-17) are shown in Fig. 1; only copolarized channels (S_{HH} and S_{VV}) are considered since the cross-polar returns are corrupted by the thermal noise. Data takes TSX-4, TSX-7, and TSX-17 correspond, respectively, to high-, medium-, and low-SNR scenarios, with mean values of 16.3, 10.9, and 3.7 dB for the copolar S_{HH} channel. The average SNR estimated values are summarized in Table II for the different data takes, where the cross-polarized returns have low SNR (most of them around 1–5 dB). Data takes TSX-11 and beyond (incidence angle above 36°) have a higher impact of the thermal noise, as indicated by the reduced SNR conditions, even for the copolar channels. For TSX-4 [see Fig. 1(a) and (b)], the local surface wind produces an

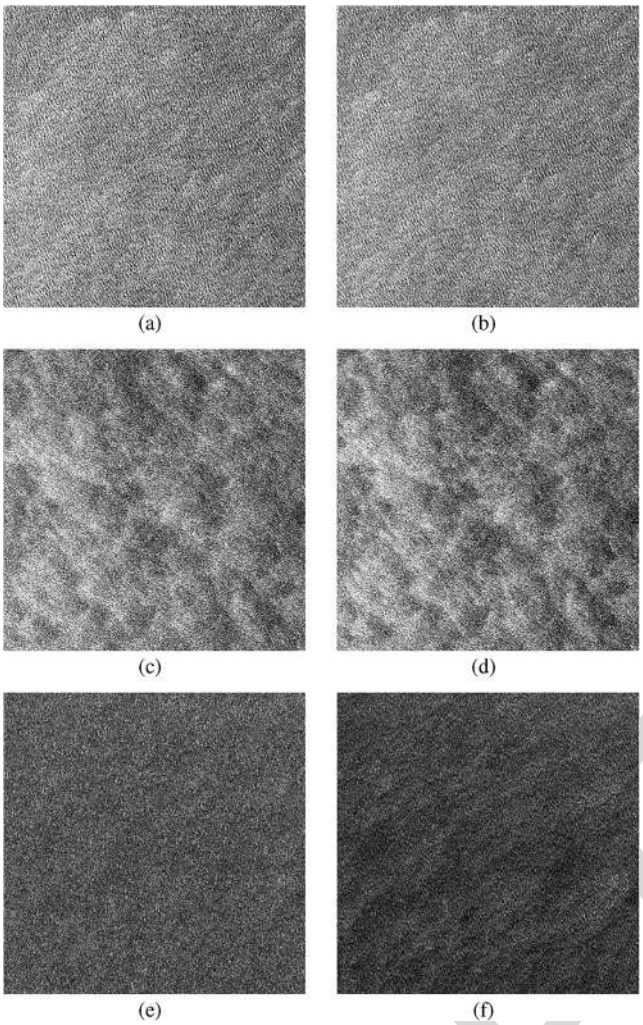

Fig. 1. Multilook (11 × 11) patches (512 × 512 pixels). (a) and (b) S_{HH} and S_{VV} for TSX-4 ($v_{\mathrm{win}} = 6.3$ m/s and $\theta_{\mathrm{win}} = 331°$). (c) and (d) S_{HH} and S_{VV} for TSX-7 ($v_{\mathrm{win}} = 6.9$ m/s and $\theta_{\mathrm{win}} = 62°$). (e) and (f) S_{HH} and S_{VV} for TSX-17 (no wind information).

TABLE II
ESTIMATED SNR AVERAGE VALUES FOR THE TSX DATA TAKES

ID	γ [deg]	SNR [dB]			
		S_{HH}	S_{VV}	S_{HV}	S_{VH}
TSX-1	19.85-21.74	23.0	-	4.8	-
TSX-2	22.43-24.26	19.6	-	4.3	-
TSX-3	23.75-25.49	17.7	17.9	6.8	6.9
TSX-4	23.75-25.49	16.3	16.5	5.9	6.1
TSX-5	24.80-27.99	11.7	-	-	-
TSX-6	29.70-31.30	8.7	9.9	3.8	4.0
TSX-7	29.70-31.30	10.9	11.6	4.2	4.3
TSX-8	30.81-32.33	9.2	-	4.0	-
TSX-9	31.91-33.42	9.1	-	4.1	-
TSX-10	33.04-34.50	6.5	8.6	0.9	1.3
TSX-11	36.18-37.54	5.1	6.6	2.6	2.6
TSX-12	36.18-37.54	5.3	6.2	3.2	3.3
TSX-13	39.03-40.29	6.4	8.9	2.8	3.4
TSX-14	40.02-41.25	5.8	8.8	2.6	3.4
TSX-15	40.02-41.25	3.5	4.5	2.5	2.4
TSX-16	43.45-44.58	2.8	-	2.2	-
TSX-17	44.37-45.48	3.7	6.2	2.3	2.4

appreciable wave pattern. For TSX-7 [see Fig. 1(c) and (d)], a more turbulent scenario is observed with a front propagating mainly in the diagonal direction. Turbulence, such as eddies or upwellings, could produce such response, bringing also some organic material (surfactants) to the surface [17]. At the highest incidence angle region, i.e., TSX-17, the HH channel has a noise-like pattern [see Fig. 1(e)] compared with VV [see Fig. 1(f)], where a wave pattern is roughly appreciated.

Ground truth data from the historical database of the National Data Buoy Center of the National Oceanic and Atmospheric Administration and the Canadian Moored Bouy of the DFO are available only for some acquisitions, as indicated in Table I. The geographical location of the employed buoys matches the center of the acquired images, but the temporal sampling rate is not sufficient to determine the exact sea conditions. Typical differences on time are between 30 and 60 min before or after the acquisition time; however, in most cases, sea conditions are quite stable in a 4-h window around the acquisition time.

III. SEA CLUTTER CHARACTERIZATION METHODOLOGY

A software module has been implemented to automatically perform a complete and exhaustive characterization of the data based on the three-level approach (radar backscattering coefficient,[2] statistics, and polarimetry). This analysis module can accept as input a set of different data takes from different sensors, where each is processed sequentially.

The first submodule performs a radiometric calibration, based on the input product information as described in [18], such that the intensity of the pixels at its output is related to σ^0 values.[3] In the next block, the area of interest (AOI) is selected, which is, to date, carried out simply by a visual inspection of the image product considering a rectangular AOI. Afterward, a subregion characterization based on a sliding window over this very AOI is performed. It is possible to define the size of such a sliding window and the overlapping in both range and azimuth dimensions.

For the statistical characterization and the normalized reflectivity σ^0 estimation, a window considering the whole azimuth strip for each range bin (range line basis) within the AOI has been selected. Therefore, the dependence of different descriptors with the incidence angle can be studied. For polarimetric decomposition, a rectangular sliding window of 11 × 11 without overlapping has been used to avoid mixing different scattering mechanisms and obtain adequate speckle filtering [19]. As proposed in [5], an additive noise filtering (NF) (for quad-pol data) can be performed in order to reduce the noise impact. Then, the polarimetric description is performed before and after NF.

Prior to sub-AOI dependent characterization, specific filtering on the data can be optionally completed,[4] such that the impact of man-made structures present in the open sea (such as vessels, oil platforms, and wind farms) is minimized, avoiding

[2]In the literature, the radar backscattering coefficient is also referred as normalized radar cross section (NRCS).

[3]It must be noted that those pixels with negative intensities, once the calibration is performed, are excluded from the subsequent characterization.

[4]This filtering method has been considered only for those data takes where a high density of high-reflectivity man-made targets is expected, based on a visual prescreening approach, taking into account the *a priori* geographical location of the region being analyzed; otherwise, and depending on the filtering threshold, the sea clutter data characterization could be impaired.

corruption of the data analysis. A simple filter approach has been implemented: those pixels, whose magnitude y_i

$$y_i \geq \mu_{\mathrm{subAOI}} + \beta\sigma_{\mathrm{subAOI}} \quad (1)$$

exceeds the mean statistical value μ_{subAOI} in a given number of times β the standard deviation σ_{subAOI}, are discarded. Both statistical moments are estimated from the available samples within the sub-AOI, whereas the β term is experimentally adjusted, with typical values between 2 and 6.

IV. Radiometric Analysis (NRCS)

Most of the available semiempirical models of σ^0 (NRCS) are optimized for the low grazing region, based on ground-based radar observations. Therefore, they are not applicable for spaceborne SAR acquisitions typically at 20°–45° of incidence angle. Recently, two models have been proposed: the first one, the Naval Research Laboratory (NRL) [20], is based on the Nathanson reference tables in [21], covering the region of 30°–90°; the second one, named XMOD2 [6], has been optimized from TSX/TDX copolar data, for incidence angles from 20° to 45°. XMOD2 provides σ^0 values at VV, and thus, PR models should be used to retrieve the HH component. In [6], three models (T-PR, E-PR, and X-PR) have been adjusted for copolarized TSX data.

The estimated σ^0 for the different data takes is depicted as a function of the incidence angle in Fig. 2 for the copolar channels. A sliding window in a range line basis is used, i.e., σ^0 is averaged using all the azimuth samples in a range bin. The sea return decreases as a function of incidence angle, where the S_{VV} channel has, in general, a higher backscattering than S_{HH}. Cross-polar channels, not reported due to space limitations, have low σ^0 values, close to noise level. NESZ is also reported for the different data takes as dotted black lines in Fig. 2, which can help in understanding the impact of the thermal noise on each data take and thus the related SNR metric (estimated average values are reported in Table II). Comparing the NESZ of quad-pol data with dual-pol acquisitions (e.g., TSX-6 versus TSX-8), a degradation around 3 dB is observed due to the DRA mode operation. Therefore, the increase on NESZ (or decrease in SNR) for quad-pol data will impair the proper characterization of the sea clutter using TSX data. For some data takes (e.g., TSX-11, TSX-12, TSX-15, and TSX-16), and due to their reduced SNR conditions (≈2–5 dB), the effect of the antenna elevation pattern at the edges of the corresponding subswath can be clearly appreciated.

In Fig. 2, the range of copolar values predicted by the NRL and XMOD2 models for a sea surface wind speed range of 0.1–20 m/s is indicated by the shaded regions, delimited by dash–dot–dot and dashed gray lines, respectively. In the XMOD2 case, an average of the upwind, crosswind, and downwind conditions has been considered. Moreover, the expected values for HH have been also averaged for the different PR models (T-PR, E-PR, and X-PR). For data takes with ground truth information, the NRL model has an average deviation w.r.t. the estimated values of 6.92 and 5.11 dB for S_{VV} and S_{HH} channels, respectively; whereas XMOD2 presents a mean error of 0.98 dB for S_{VV}; and for the S_{HH} channel, the average deviations are 1.12, 1.23, and 2.63 dB for T-PR, E-PR, and X-PR, respectively. This divergence between the VV and HH returns (also among the different PR models) has been observed when retrieving wind speeds from TSX/TDX VV-only data and HH-only data as noted in [6], exploiting XMOD2 and PR models.

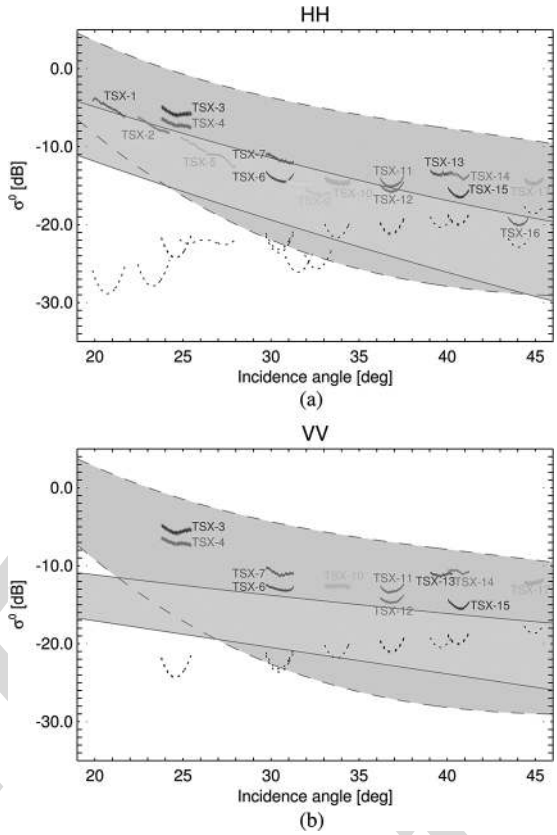

Fig. 2. Estimated σ^0 as a function of the incidence angle, using a sliding window in a range line basis with no overlap. (a) HH. (b) VV. The different data takes correspond to different colors; the (dotted black line) estimated NESZ is also plotted, and the shaded regions represent the predicted values from the NRL (delimited by dash–dot–dot lines) and XMOD2 (delimited by dashed lines) models, for a wind speed variation of 0.1–20.0 m/s (average value between upwind, crosswind, and downwind is performed for XMOD2 and an average over the different PR models for HH extraction).

Since the available information of the sea conditions does not correspond precisely to the time of acquisition, some error could be introduced in the inversion of σ^0 for the theoretical models. The NRL parametrization uses only two Nathanson tables [21], at 30° and 60° of incidence angle, whereas five tables are used to model reflectivity at incidence angles greater than 80° [20]. Therefore, a degradation in properly modeling σ^0 is expected when considering typical spaceborne geometries with 20°–45°.

In case of XMOD2, which agrees much better with the estimated values, the source of discrepancy should be also related to the fact that this model has been optimized for a given set of TSX/TDX copolarized acquisitions, not for quad-pol data. Moreover, the quality of such experimental data (DRA operation) should be carefully reviewed, particularly taking into account that some calibration issues have been highlighted when retrieving the fore and aft signals from the sum and difference ones [4]. The calibration procedure proposed in [4] has been applied for the along-track interferometric mode, where the receive polarizations of the two halves of the antenna

TABLE III
STATISTICAL DISTRIBUTIONS USED TO FIT THE SEA CLUTTER AMPLITUDE Y (REFERENCES TO THE ESTIMATION METHODS ARE INDICATED)

Distribution	Probability density function (PDF)	Parameters	Ref.
Log-normal	$p_Y(Y) = \frac{1}{Y\sqrt{2\pi\sigma^2}} \exp\left(-\frac{(\ln Y-\mu)^2}{2\sigma^2}\right)$	μ (location) σ (scale)	[12]
Weibull	$p_Y(Y) = \beta \frac{Y^{\beta-1}}{a^\beta} \exp\left(-\left(\frac{Y}{a}\right)^\beta\right)$	β (shape) a (scale)	[22]
K-distribution[1]	$p_Y(Y) = \frac{4b\frac{(v+1)}{2}}{\Gamma(v)} Y^v K_{v-1}\left(2Y\sqrt{b}\right)$	v (shape) b (scale)	[23] [24]

[1] $\Gamma(\cdot)$ is the gamma function and $K_n(\cdot)$ refers to the modified Bessel function of second kind and order n.

are the same, but no investigations have been made for the quad-pol case (different polarizations in the fore and aft halves). Hence, and as stated in the TSX product specification [7], the DRA specific instrument characteristics have to be further investigated for full calibration. From these results, it is clear that an optimization of the XMOD2 and different PR models is needed for quad-polarized data, using a wide data set with *in situ* buoy measurements and considering further efforts in instrument calibration for the fully polarimetric operation.

V. STATISTICAL ANALYSIS

For low-resolution radars and grazing angles typically above 10° (incidence angles less than 80), the amplitude (or magnitude) statistics of the sea returns have a "speckle"-like pattern [8], [11], i.e., Rayleigh distributed in amplitude. For higher resolution systems, the statistical description of the echo returns deviates from the Gaussian hypothesis, having a target-like response with more heavy-tailed distributions [8], [11]. This non-Gaussian clutter has been commonly described, among others, by log-normal and Weibull distributions [12], [13]. K-distribution, which provides also a good description of the sea clutter magnitude for high-resolution radars [8], [11], has been theoretically justified on the basis of the *compound model* [8].

Table III lists the probability density functions (PDFs) and the related parameters for the log-normal, Weibull, and K distributions. Y refers to the amplitude (absolute value) of the single-look ith polarimetric channel S_i (complex data), either S_{HH}, S_{VV}, or S_{HV} (polarization states in reception and transmission are indicated by the first and second subindexes, respectively).

Fig. 3(a) and (b) show the fitting of the considered distributions (K, Rayleigh, log-normal, and Weibull) to the S_{HH} channel's magnitude for data takes TSX-4 and TSX-17, respectively, which correspond accordingly to high-SNR (16.3 dB) and low-SNR (3.7 dB) scenarios. Only the results for a specific single sub-AOI are shown, i.e., in this case, the data distributions are computed using all the azimuth samples for a specific single range bin. The distributions are plotted on a semilogarithm scale, i.e., the clutter is expressed in decibels, which, for calibrated data, refers to σ^0 (theoretical distribution fitting and parametric estimation done in the linear domain).

For TSX-4, in the small incidence angle region, K-distribution (dotted blue line with circle markers) fits best the data distribution (solid red line), particularly in the distribution's tail. This is crucial, for instance, in GMTI operation, since the tail's shape determines the detection threshold for a given false alarm rate. Weibull distribution shows good agreement with the data only for smaller σ^0 values, whereas the log-normal does not fit the data distribution. Similar results are obtained for the S_{VV} channel. In the cross-polar channel S_{HV}, the three distributions (K, Rayleigh, and Weibull) collapse to a complex Gaussian distribution mainly due to the noise impact. For TSX-17, the reduction in SNR, in comparison with TSX-4, leads to a major contribution of the thermal noise, which is translated into a more Gaussian-like data distribution. This behavior can be recognized from the statistical fitting in Fig. 3(b), where the K- and Weibull distributions tend to a Rayleigh one, i.e., shape parameters $v > 30$ and $\beta \approx 2$, accordingly. For the S_{VV} channel, there is an increase around 3 dB in SNR compared with HH polarization, and K-distribution slightly departs from Gaussianity, fitting best the data.

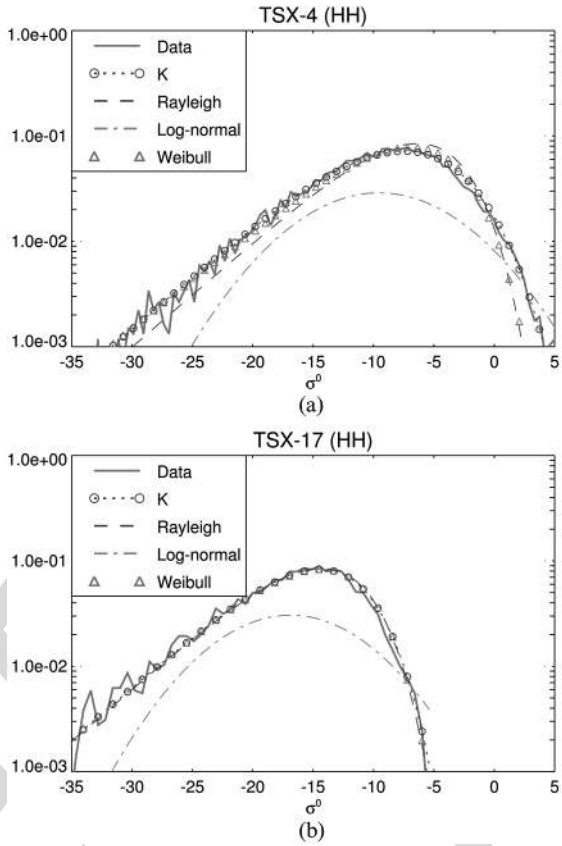

Fig. 3. Fitting of theoretical distributions (K, Rayleigh, log-normal, and Weibull) to the S_{HH} channel's magnitude (within a specific sub-AOI) for data takes (a) TSX-4 [SNR of 16.3 dB] and (b) TSX-17 [SNR of 3.7 dB].

A good metric that allows deciding whether the data under analysis are spikier or tend to a Gaussian distribution is the shape parameter of the K-distribution, i.e., v. In Fig. 4, this parameter is shown as a function of incidence angle for the different data takes and copolar channels.[5] Blacknell's method has been used to estimate the shape and scale parameters of the K-distribution. Similar results have been obtained using the *fractional moments* method [23].

In the S_{HH} channel [see Fig. 4(a)], and for incidence angles between 20° and 33°, the shape parameter v has a range of

[5]For those data takes at incidence angle above 35° and with reduced SNR, only TSX-13 and TSX-14 are shown in Fig. 4 for clarity in the representation.

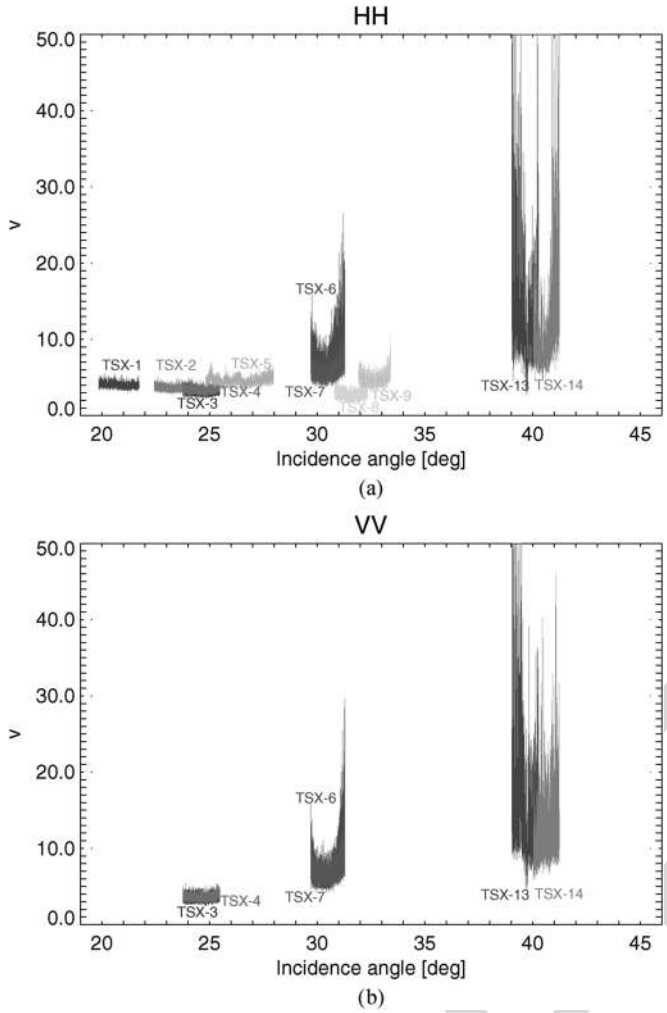

Fig. 4. Estimated shape parameter for a K-distributed amplitude fitting of the data as a function of the incidence angle, using a sliding window in a range line basis with no overlap. (a) HH. (b) VV. The different data takes are color-coded as in Fig. 2 (shape parameter estimated using Blacknell's approach).

3–10, with contained variation for each data take. For incidence angles greater than 36°, the values of the shape parameter are above 10, with much higher dispersion, related to the reduction in SNR as incidence angle increases [see Fig. 2(a) and Table II]. This is quite evident for TSX-16 and TSX-17, where noise impact produces a variation on the shape parameter from 10 to 1000. For VV polarization [see Fig. 4(b)], similar trends are observed, but in this case, the higher sea clutter returns in the high incidence region reduce the shape parameter dispersion on data take TSX-17, with values between 5 and 20. Comparing the shape parameters of the polarimetric channels, different values are obtained showing that the scalar product model (on which K-distribution is based) can be extended to a multivariative product model, associating an individual texture variable per polarimetric channel. For the cross-polar channels, high values of the shape parameter are obtained with a high dispersion due to the low sea backscattering contribution (close to NESZ).

One way to quantitatively evaluate the non-Gaussian behavior of the data is by computing the NIM of the nth order [8], i.e.,

$$\text{NIM}_n = \frac{E\{Z^n\}}{E^n\{Z\}} \tag{2}$$

where Z refers to data intensity (or power), i.e., $Z = Y^2$, being $Y = |S_i|$ the magnitude, and $E\{\cdot\}$ is the expectation operator. Values of the nth-order NIM above $n!$ (Gaussian limit) are indicators of spiky data.

In general, and for the copolar channels, the estimated NIM (as a function of the estimated K-distribution shape parameter v) follows quite good the theoretical K-distribution NIM trend, for the third and fourth orders, when considering small to medium values of v (< 10), i.e., spikier clutter returns. Therefore, the compound model theory that supports the K-distribution is able to describe the mechanism, which results from a combination of Bragg scattering (from resonant capillary waves) and whitecap scattering originated from breaking waves [8]. The presence of the latter phenomena is known to increase the spikiness of the clutter returns [8], associated to smaller values of v as observed for data takes with incidence angle below 30°, with medium to high SNR conditions (> 10 dB), as indicated in Table II.

Analogously, the estimated third- and fourth-order NIM have been compared with the theoretical ones for Weibull and log-normal distributions. Weibull presents, generally, a worse matching with the theoretical trends for the copolar channels compared with the K-distribution. When considering a log-normal distribution fitting, a very poor matching between the estimated NIM and the theoretical ones is obtained. In summary, K-distribution provides good fitting for specific TSX acquisitions over the sea, particularly for low incidence angles, where SNR conditions are favorable (> 10 dB). In this region, the lowest values of the K-distribution shape parameter are obtained, indicating a much spikier behavior of the data, which can be also related to the higher contribution of breaking wave events, as analyzed in Section VI.

K-distribution is among one of the statistical distributions used to model and describe non-Gaussian statistics, based on the well-known compound model. Under this hypothesis, the complex signal can be characterized as a product between the square root of a random variable T (representing the texture) and an independent zero-mean complex Gaussian random process ("speckle"). In this sense, the computation of the so-called *log-cumulants* is very useful to evaluate the presence of texture, i.e., non-Gaussian statistics [9]. Such analysis is typically performed through the log-cumulant diagram [9], [10], where the second κ_2 (variance) and third κ_3 (skewness) log-cumulants are plotted against each other. These *log-moments* are computed as [10]

$$\begin{aligned} \kappa_2 &= m_2 - m_1^2 \\ \kappa_3 &= m_3 - 3m_1m_2 + 2m_1^3 \end{aligned} \tag{3}$$

where m_n is the log-moment of order n, i.e., $m_n = 1/L \sum_{l=1}^{L} (\log Z_l)^n$, where L intensity samples have been used.

Fig. 5 shows the log-cumulant diagram for the three representatives acquisitions considered in Fig. 1 (from near to far incidence angle regions). These plans are covered by five (texture) distribution families, namely, Gamma (dash–dotted line modeling a K-distribution in amplitude), inverse Gamma (dashed black line), Beta (light gray shaded region), inverse

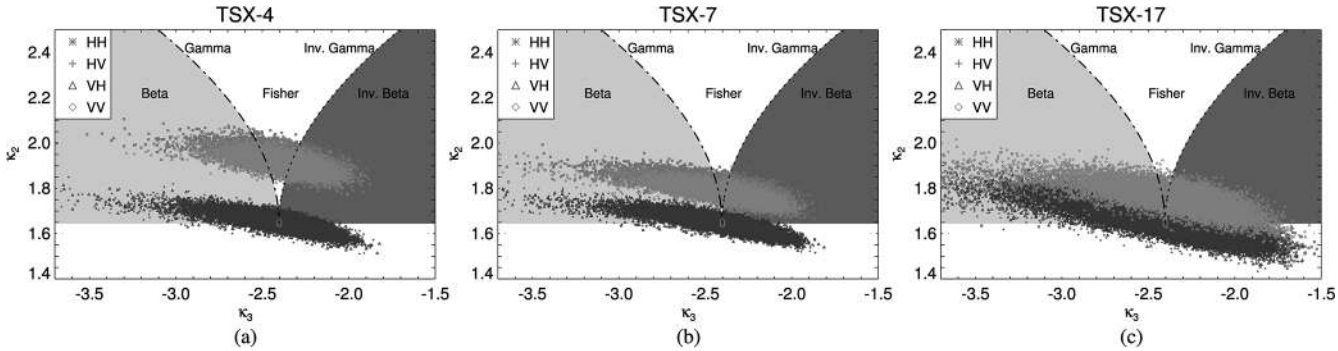

Fig. 5. Log-cumulant diagrams for different data takes: (a) TSX-4, (b) TSX-7, and (c) TSX-17. A sliding window in a range line basis with no overlap has been used (HH as red "x," HV as green "+," VH as "△," and VV as gold "◇").

Beta (gray shaded region on the right), and Fisher (region in between). The intersection point between these distributions corresponds to no texture at all, i.e., Gaussian statistics.

The results in Fig. 5 are in line with the previous statistical analysis: for TSX-4, in the near incidence angle region, the copolar channels lie higher up in the diagram compared with the cross-polar channels, indicating a deviation from Gaussian statistics (spikier response). As the incidence angle increases, the copolar channels move to lower regions in the diagram (less texturized). For TSX-17, with the highest incidence angle, VV has more texture compared with HH, as expected from the K-distribution shape parameter study.

VI. Analysis of the Polarimetric and Scattering Features

A. SAR Polarimetry

A polarimetric SAR (PolSAR) system measures the scattering matrix, which, for the monostatic case and on the Pauli basis, can be expressed in vectorial notation as

$$\mathbf{k} = \frac{1}{\sqrt{2}}[S_{\mathrm{HH}} + S_{\mathrm{VV}} \quad S_{\mathrm{HH}} - S_{\mathrm{VV}} \quad 2S_{\mathrm{HV}}]^T \tag{4}$$

where $(\cdot)^T$ refers to the transpose operator, and S_i are the complex data of the ith polarimetric channel. The distribution of $\mathbf{k}$ is completely described by the Hermitian positive definite coherency matrix $\mathbf{T} = E\{\mathbf{k}\mathbf{k}^H\}$ under the Gaussian assumption [25], where $(\cdot)^H$ is the transpose and complex conjugate operator.

The coherency matrix $\mathbf{T}$ is estimated from the data, such that the speckle noise is filtered. The maximum-likelihood estimator can be obtained as a spatial averaging (boxcar or multilook filter)

$$\widehat{\mathbf{T}} = \frac{1}{L}\sum_{i=1}^{L} \mathbf{k}_i \mathbf{k}_i^H \tag{5}$$

where L refers to the number of looks or samples employed in the estimation of $\mathbf{T}$, and $\mathbf{k}_i$ is the vector in the Pauli basis for the ith sample.

B. Features Definition

The main objective of the polarimetric study is to analyze the scattering properties of the sea surface observed by the high-resolution X-band TSX sensor. This way, two different sets of polarimetric features are considered. First, the eigendecomposition of the coherency matrix allows extracting roll-invariant parameters, such as the entropy H, anisotropy A, and mean alpha angle $\overline{\alpha}$, as originally proposed by Cloude and Pottier [14]. H measures the randomness of the scattering mechanism, $\overline{\alpha}$ provides physical information about the type of average scatter, and A (complementary to H) measures the relative significance of the second and third eigenvalues. The $H/A/\overline{\alpha}$ features allow a physical interpretation of the PolSAR data, and thus, their correct estimation provides a reliable prediction of physical parameters [5], [14]. This eigendecomposition-based analysis has been successfully applied over the oceans to determine polarimetric scattering mechanisms and for discrimination/classification of different types of slicks [16], [26], [27].

To complement the eigendecomposition-based analysis, additional polarimetric features exploiting the intensity of the copolarized channels have been used, based on the σ^0 model proposed by Kudryavtsev *et al.* [15]. As analyzed in [15], [28], and [29], the Bragg theory is not fully able to explain and represent the backscattering from the ocean, due to the existence of sea spikes (in high-resolution radar data), which induce large deviations of observed PR compared with the theoretical Bragg one. This suggested that some mechanism supporting non-Bragg scattering and connected with breaking waves also contributes to the NRCS from the sea. The proposed NRCS model in [15] is a superposition (in linear units) of a regular sea surface, polarized component related to the Bragg scattering (σ_{pp}^{0B}), and surface areas with enhanced roughness produced by breaking waves, nonpolarized component linked to non-Bragg scattering (σ_{pp}^{0nB}), i.e., $\sigma_{pp}^{0} = \sigma_{pp}^{0B} + \sigma^{0nB}$. It is assumed that the nonpolarized component is the same for both copolar channels.

As anticipated by several studies [15], [28], [29], the contribution of the nonpolarized radar returns to the total NRCS can be considerable, mainly due to the presence of breaking waves. As suggested in [15] and [29], the computation of the PR

$$\mathrm{PR} = \frac{\sigma_{\mathrm{HH}}^{0}}{\sigma_{\mathrm{VV}}^{0}} = \frac{\sigma_{\mathrm{HH}}^{0B} + \sigma^{0nB}}{\sigma_{\mathrm{VV}}^{0B} + \sigma^{0nB}} \tag{6}$$

is an indicator of the presence of significant wave breaking (PR ≈ 1), deviating from the PR for the Bragg component $p_B = \sigma_{\mathrm{HH}}^{0B}/\sigma_{\mathrm{VV}}^{0B}$. In this paper, p_B is computed as the ratio

between the perpendicular ($B_\perp$) and parallel ($B_\parallel$)[6] Bragg scattering coefficients according to [5]. It must be noted that the effect of slope of the long tilting waves on the NRCS is higher at the HH polarization than in VV, particularly at large incidence angles [15], and hence, this could lead to an increase in PR not directly related to the breaking waves. Nevertheless, it is complicated to separate the effect of breaking waves from tilting waves, since, in the formation process of the former ones, there is a progressive increase of the slope (generation of a sloping wave front) correlated with a temporal increase of the surface roughness [16]. In this sense, further studies are required to carefully analyze the impact of both tilting and breaking waves, trying to separate both processes.

C. X-Bragg and Extended X-Bragg (X2-Bragg) Models

It has been generally assumed that the radar sea echo returns are mostly dominated by Bragg surface scattering; however, some depolarization has been observed, as noted in [16], [26], and [30]. Such nonpolarized returns have been found to significantly contribute to the sea backscattering due to breaking waves (increasing surface roughness), as analyzed in [15], [28], and [29], particularly when increasing the frequency of operation (and thus the resolution) [15].

Under these considerations, the application of the small perturbation model (SPM) for the polarimetric scattering analysis would be too simplistic, as its validity range is limited to small surface roughness conditions [5]. Therefore, the evaluation of the X-Bragg model, originally proposed by Hajnsek *et al.* [5], seems to be more reasonable, since it is a two-component model, including a Bragg scattering term and a roughness induced rotation symmetric disturbance. This way, depolarization (nonpolarized components) and cross-polarized backscattering effects are included. As proposed in [5] and [16], this can be obtained modeling the surface as a reflection symmetric depolarizer, randomly rotating the Bragg coherency matrix $\mathbf{T}$ about an angle β w.r.t. the local surface normal and averaging it over a statistical distribution $p_\beta(\beta)$. For a uniform distribution $p_\beta(\beta)$ with zero mean and width β_1, the coherency matrix can be expressed by [5]

$$\mathbf{T} = m_s^2 \begin{bmatrix} C_1 & C_2\mathrm{sinc}(2\beta_1) & 0 \\ C_2^*\mathrm{sinc}(2\beta_1) & C_3\,(1+\mathrm{sinc}(4\beta_1)) & 0 \\ 0 & 0 & C_3(1-\mathrm{sinc}(4\beta_1)) \end{bmatrix} \tag{7}$$

where m_s is the backscatter amplitude related to the surface roughness; sinc function refers to $\mathrm{sinc}(x) = \sin(x)/x$; and the coefficients C_1, C_2 and C_3 can be expressed in terms of $B_\perp$ and $B_\parallel$ [5]. These coefficients depend on the incidence angle γ and the dielectric constant $\epsilon = \epsilon' - \jmath\epsilon''$. The latter can be obtained from the model developed by Klein and Swift [31].

The width of the distribution β_1 models the roughness disturbance of the surface and controls the level of cross-polarized power and the polarimetric $(S_{\mathrm{HH}} + S_{\mathrm{VV}})(S_{\mathrm{HH}} - S_{\mathrm{VV}})$ coherence [5]: for $\beta_1 = 0^\circ$ (smooth surface), the cross-polarized power is zero, and there is no depolarization effect (corresponding to the "pure" Bragg or SPM model); with increasing β_1 (increasing roughness), the HV term increases, and the $(S_{\mathrm{HH}} + S_{\mathrm{VV}})(S_{\mathrm{HH}} - S_{\mathrm{VV}})$ coherence decreases until 0 in the high roughness limit case of $\beta_1 = 90^\circ$ (azimuthally symmetric surface). The breaking waves produce a temporal increase in the surface roughness [8], [16], and this could be related to an increase also in the β_1 term of the X-Bragg model. In fact, this model has been used to derive a description of the polarimetric behavior of a breaking wave, as presented in [16]. Therefore, it is interesting to evaluate the applicability of the X-Bragg model to SAR polarimetric sea data, which can be useful for future studies trying to invert some geophysical parameters of the ocean using polarimetric data.

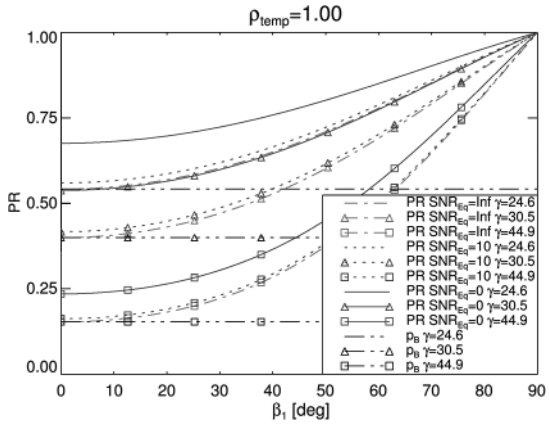

Fig. 6. PR of the X-Bragg ($\mathrm{SNR_{Eq}} = \infty$) and X2-Bragg models is represented as a function of the roughness β_1 parameter for different incidence angles γ and different noise conditions $\mathrm{SNR_{Eq}}$ (an X-band system at 9.65 GHz, a sea temperature of 10 °C, and salinity of 35‰ are considered).

The DRA acquisition mode [4], employed to obtain fully polarimetric images with an along-track interferometric configuration, has a two-folded impact on measured data. On one hand, as the receive antenna is halved, a direct consequence is a reduction on the received gain, which translates into higher values of NESZ. On the other hand, the alternate transmission of horizontal and vertical polarizations in a pulse-by-pulse basis jointly with the along-track configuration (to receive simultaneously H and V) produces a temporal lag between different pairs of channels. The different polarimetric channels should be spatial aligned (coregistered), such that they observe the scene from the same positions but at different times. During this time lag, around $\tau_{\mathrm{coreg.}} = 1$ ms for TSX S_{HH} and S_{VV} channels (or S_{HV} and S_{VH}), the sea backscattered field decorrelates due to internal clutter motion. Typical decorrelation times of the sea are between 8 and 10 ms for wind speeds of 15 m/s down to 5 m/s, [32]. For an X-band system at VV, the temporal coherence ρ_{temp} could be between 0.9 and 1.0 for a time lag around 1 ms, [32]. From the results presented in Section VI-D for TSX quad-pol, it has been observed that both the noise level and the sea clutter temporal decorrelation should be accounted for in the X-Bragg model to properly characterize the sea clutter in polarimetric terms. Taking into account these issues, the X-Bragg model has been extended to the X2-Bragg model (extended-extended Bragg). The mathematical derivation of the X2-Bragg

[6]Note that, here, perpendicular and parallel are referenced w.r.t. the incidence plane.

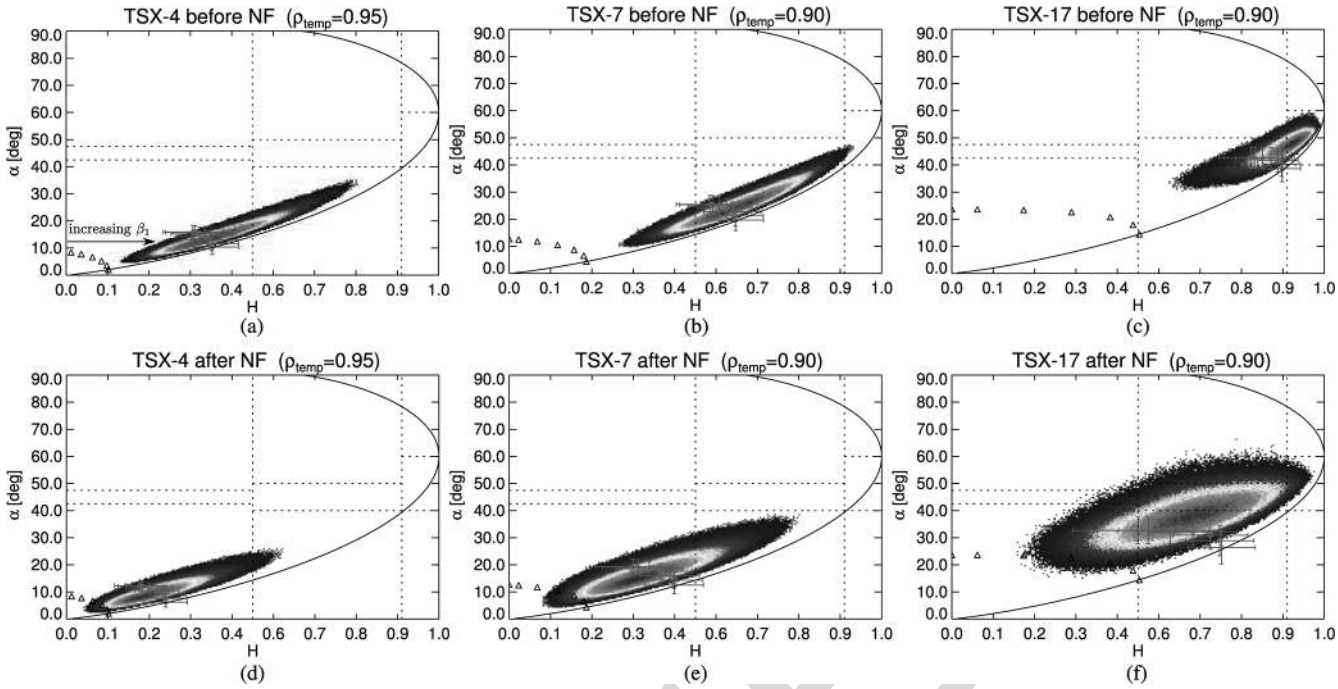

Fig. 7. Two-dimensional distributions on $H/\overline{\alpha}$ plane for different data takes (TSX-4, TSX-7, and TSX-17, from left to right), including the theoretical X/X2-Bragg models (β_1 variation from 0° to 90° and single dielectric constant for standard sea conditions of 10 °C and salinity of 35‰); black triangles refer to the original X-Bragg model, and magenta diamonds correspond to the X2-Bragg model (error bars/standard deviations in $H/\overline{\alpha}$ are included): (a)–(c) before and (d)–(f) after NF. (a) and (b) TSX-4 with $\rho_{\rm temp} = 0.95$. (b) and (e) TSX-7 with $\rho_{\rm temp} = 0.90$. (c) and (f) TSX-17 with $\rho_{\rm temp} = 0.90$.

and a theoretical evaluation for different system/scenario conditions are presented in Appendixes A and B, respectively.

In Fig. 6, the PR of the X-Bragg ($\mathrm{SNR_{Eq}} = \infty$) and the X2-Bragg is plotted as a function of β_1 for different incidence angles γ and effective[7] signal-to-noise ratio $\mathrm{SNR_{Eq}}$ conditions (no temporal decorrelation has been considered). The horizontal lines correspond to the PR for Bragg components p_B. It can be seen how the PR approaches p_B for β_1 close to zero (pure Bragg) and increases to higher values as roughness condition increases, with a value of 1 for complete depolarized scattering. From [15] and [29], this trend can be related to higher contribution of breaking wave events, which induce higher roughness conditions. It must be also noted that, as the noise contribution increases, there is also an increase in the PR, since the noise is a common nonpolarized term affecting both copolar channels.

D. Experimental Results

An analysis of the scattering plots in the $H/\overline{\alpha}$ plane has been carried out for the different data takes, without and with additive NF as proposed in [5]. Fig. 7 shows these 2-D distributions for the three representative data takes (near to far incidence, from left to right). Before NF, the dominant mechanism moves from low entropy surface scattering[8] at near incidence [see Fig. 7(a)], passing by medium entropy surface scattering [see Fig. 7(b)], ending up to high entropy region characterized by random anisotropic scatters [see Fig. 7(c)], caused by the higher noise contribution. Comparatively, NF produces a reduction both in H and $\overline{\alpha}$, leading to a dominant scattering in the low entropy surface zone ($H < 0.5$ and $\overline{\alpha} < 40°$) for data takes with incidence angle below 36° (e.g., TSX-4 and TSX-7).

The distributions of the eigenvalues in Fig. 8 for the three reference data takes are a good visual indicator of the polarimetric mechanisms' evolution as a function of incidence angle. In Fig. 8, the lowest eigenvalue (λ_4) has been also included since it provides information on the expected noise floor, such that the dominant mechanism's relative contribution with respect to the noise can be easily tracked. For TSX-4 [see Fig. 8(a)], there is a clear dominant mechanism (λ_1), surface scattering, as observed from the α_1 distribution in Fig. 9(a), centered around 5°. As incidence angle increases, the first eigenvalue decreases. At the farthest available incidence angle (TSX-17) [see Fig. 8(c)], no clear dominant mechanism is present, being the distributions of the eigenvalues closer to each other, such that a noise-like mechanism is expected in accordance with the σ^0 and statistical characterizations.

In general, the second mechanism almost keeps its relative strength w.r.t. noise floor independently of incidence angle. In Fig. 9, where the distributions of the individual α parameters are shown, the related α_2 with a similar trend as α_3 lies between 70° and 90°. These values are representative of double-bounce scattering, less probable in the sea backscattering. Considering the X-Bragg model extension to account only for thermal noise impact, parameters associated to the second mechanism do not agree with the observations from experimental data: on one hand, α_2 corresponds to 90° independently from β_1 and $\mathrm{SNR_{Eq}}$; on the other hand, the expected level of λ_2 is much closer to λ_3 than that observed from real data. These considerations reinforce the need to include also the impact of sea clutter temporal decorrelation between the polarimetric

[7]Please refer to Appendix A for further details on the definition of this equivalent $\mathrm{SNR_{Eq}}$.

[8]This region corresponds to zone 9 as designated by Cloude and Pottier [14], including surface scattering and specular scattering phenomena.

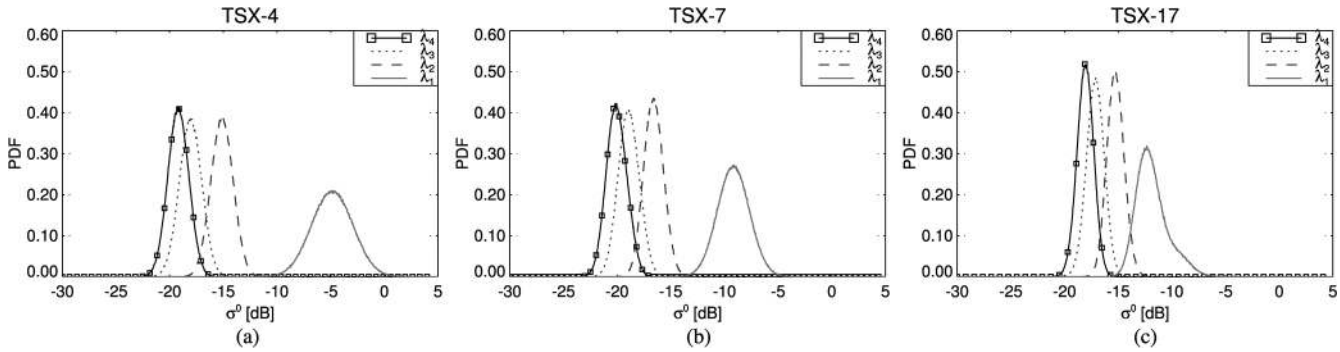

Fig. 8. Distribution of the eigenvalues, before NF, for different data takes. (a) TSX-4. (b) TSX-7. (c) TSX-17.

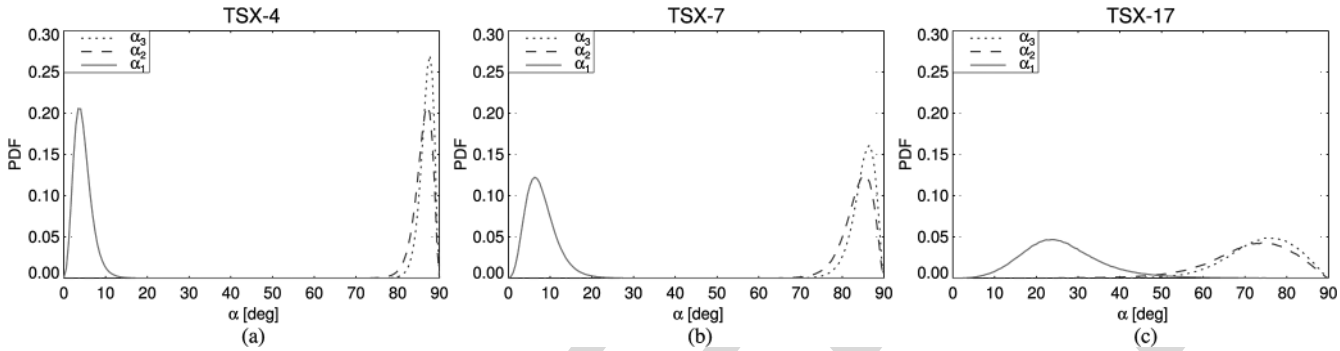

Fig. 9. Distribution of the alpha parameters, before NF, for different data takes. (a) TSX-4. (b) TSX-7. (c) TSX-17.

channels (ρ_{temp}), intrinsically related to the DRA acquisition mode itself, as proposed in the X2-Bragg model and described in Appendixes A and B.

On top of the different $H/\overline{\alpha}$ distributions in Fig. 7, the classical X-Bragg model, as black triangles, and the extended model X2-Bragg, as magenta diamond symbols, are depicted for different values of β_1 (from 0° to 90° in steps of 15°). Standard deviations are also included for the X2-Bragg model (related to $\mathrm{SNR}_{\mathrm{Eq}}$ estimation from the data). Standard sea conditions have been assumed, i.e., 10 °C and 35‰ salinity.

An important bias exists between the original X-Bragg model and the data, after and, in particular, before NF. For X2-Bragg, a much better matching between the theoretical model and the experimental data is obtained. For TSX-4 [see Fig. 7(a)], a ρ_{temp} of 0.95 provides a good matching between the theoretical extended model and the data before NF, whereas for TSX-7 [see Fig. 7(b)], this value reduces to 0.90. In case of TSX-17 [see Fig. 7(c)], a higher bias is recognized, and reducing ρ_{temp} below 0.9 does not provide any additional improvement: from the theoretical analysis of the X2-Bragg model, higher clutter decorrelation does not increase entropy for regions with $H > 0.6$. Additive noise subtraction reduces entropy from 0.92 to 0.7, but the proposed extended model predicts an average alpha value below the one observed in the data. Therefore, there might be an additional mechanism contributing to this discrepancy, which is not considered in the X-Bragg model; additional measurements with higher SNR conditions should be analyzed to support this hypothesis.

The X2-Bragg model gets close to the centroid of the data distributions in $H/\overline{\alpha}$ for values of β_1 different from zero, which means that no pure Bragg is being imaged, but there is a depolarized term contributing also to the backscattering. An increase in β_1 is related to higher surface roughness producing depolarization and an increase in the entropy. To complement the polarimetric study and gain additional insights into the nonpolarized contribution of the sea backscattering, the PR for the available quad-pol data takes is represented as a function of the incidence angle in Fig. 10. The PR p_B for the pure Bragg model is also included as solid black line.

Before NF [see Fig. 10(a)], an important difference between the estimated PR and p_B exists, which means that an important contribution on nonpolarized returns is presented, probably related to breaking wave effects. Even for the high incidence region (above 36°), where Bragg scattering is expected to be dominant, as stated in [10], an appreciable divergence between the PRs is observed (e.g., TSX-15 and TSX-17). Nevertheless, as pointed out throughout this paper, the reduced SNR conditions (≈3–4 dB) can explain this effect, since the thermal noise is also a nonpolarized component common to both copolar channels. This can be recognized from Fig. 10(b), where the difference between PR and p_B has been reduced for the high incidence angle region after NF.[9]

Following the two-component NRCS model (Bragg/non-Bragg) proposed by Kudryavtsev *et al.* [15], the relative

[9]In Fig. 10, the images have been radiometrically calibrated before the application of any further processing, i.e., the NESZ has been subtracted (in linear units) from the calibrated digital pixels, as proposed in [18]. From these results, it can be seen that there is still some residual noise that should be filtered out and that quad-pol data provide the means to do so.

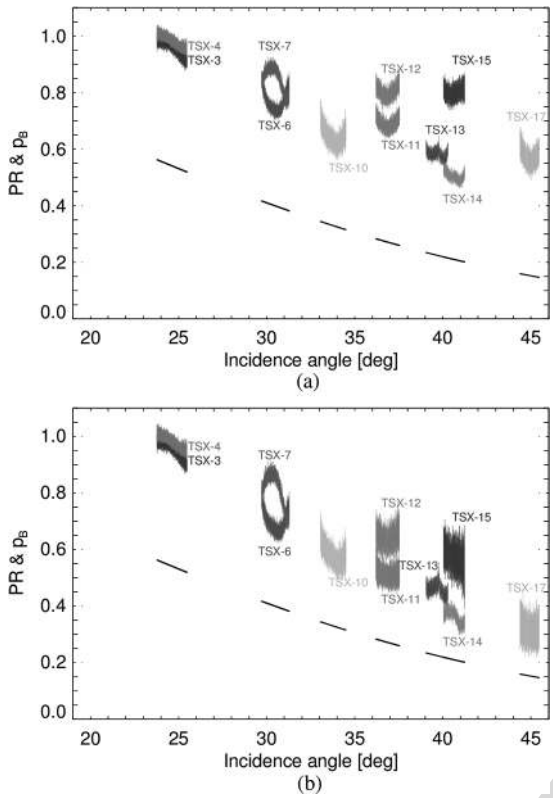

Fig. 10. PR as a function of the incidence angle for the different quad-pol data takes (color-coded as in Fig. 2): (a) before and (b) after NF; solid black lines refer to the PR for pure Bragg p_B.

contribution of the non-Bragg component with respect to the total backscattered power for the S_{HH} channel ($\sigma^{0nB}/\sigma^0_{\mathrm{HH}}$) has been computed, and it ranges from 50% to 90% (high to small incidence angles), whereas for VV, the figures ($\sigma^{0nB}/\sigma^0_{\mathrm{VV}}$) are around 20%–70%. These results are in line with the studies carried out in [15] and [29]. For TSX-3 and TSX-4, $\sigma^{0nB}/\sigma^0_{\mathrm{VV}}$ and $\sigma^{0nB}/\sigma^0_{\mathrm{HH}}$ have very similar trends close to the 90% of the total backscattered power. In this very case, with the smallest incidence angle (25°), specular returns may partially contribute to the non-Bragg scattering [10], apart from possible breaking wave effects.

A fitting of the X-Bragg and X2-Bragg models to the measured PR has been carried out. After NF, β_1 values providing the minimum average error (between the models and the data) within each quad-pol acquisition are summarized in Table IV. As described in Section VI-B, an increase in β_1 is related to a roughness enhancement and thus a higher depolarization contribution. From Table IV, it can be generally stated that β_1 reduces as a function of the incidence angle in accordance to the decrease of the nonpolarized component. For the X2-Bragg model, β_1 corresponds to the average value for three different temporal decorrelation conditions assumed in the model ($\rho_{\mathrm{temp}} = 1.0, 0.95, 0.90$). Due to the presence of thermal noise and possible temporal decorrelations, the X-Bragg model overestimates the surface roughness, when compared with the proposed X2-Bragg model, particularly for the high incidence region (above 36°).

TABLE IV
β_1 (ROUGHNESS) PROVIDING THE MINIMUM AVERAGE ERROR BETWEEN ESTIMATED PR FROM X/X2-BRAGG DATA FITTING AND MEASURED PR FOR QUAD-POL ACQUISITIONS AFTER NF

ID	X-Bragg	X2-Bragg
TSX-3	84	83.3
TSX-4	87	87
TSX-6	59	56
TSX-7	73	72
TSX-10	51	46.7
TSX-11	51	46.7
TSX-12	63	62
TSX-13	50	44.7
TSX-14	41	32.7
TSX-15	62	60.7
TSX-17	43	34.3

VII. CONCLUSION

A signal-based characterization of the sea/ocean returns imaged by TSX sensor has been carried out exploiting 17 data sets, both dual- and quad-pol. The transversal study copes with radiometric, statistical, and polarimetric analysis of the experimental data. One of the goals of this paper is to provide additional insights into proper modeling and characterization of the sea clutter response when observed by TSX.

First, the different results indicate that, for the quad-polarized data over maritime scenarios, the thermal noise impact can be a limiting factor in the correct interpretation of the TSX data, particularly for the low sea backscattering regions (incidence angles above 36°). Second, taking into account the specific DRA configuration to acquire quad-pol data, the induced temporal decorrelation of the sea returns between the polarimetric channels (due to the along-track configuration) is an additional limiting factor that should be carefully considered. This effect, combined with the additional thermal decorrelation, needs to be properly accounted for when trying to fit polarimetric physical-based models to the experimental data, in order to avoid misinterpretation. In this line, this paper proposes a new modeling approach to include such system/scenario dependent limitations applied specifically to the X-Bragg model and concreted in the new X2-Bragg model.

The NRCS analysis shows that the semiempirical model XMOD2 provides a fair fitting to the measured σ^0. Nevertheless, further studies are required to obtain a refined tunning of the XMOD2 coefficients from quad-pol TSX data sets for a wide range of sea conditions, ensuring that adequate calibration of the DRA mode can be accomplished.

Deviation from the Gaussian statistics for the TSX sea data is observed, when sufficient SNR is available and for small to medium incidence angles (below 36°). This means spikier returns and thus heavy-tailed amplitude distributions. The log-cumulant analysis shows that, for TSX, the ocean has high texture due to the higher resolution of the sensor coupled with the higher operating frequency (higher sensitivity to surface roughness variation). These results are in line with the study of the PR, which indicates an important contribution of non-Bragg scattering (depolarization), particularly for small incidence angles. As indicated in [15], [28], and [29], the presence of breaking wave events, increasing surface roughness and producing spikier returns, can explain this high depolarized

contribution. These nonpolarized returns tend to reduce as the incidence angle increases.

Exploiting the fully polarimetric information through the $H/\overline{\alpha}$ plane indicates that, for small incidence angles, the dominant scattering mechanism corresponds to low to medium random surface. The proposed X2-Bragg model proves a quite good fitting to the data in the $H/\overline{\alpha}$ plane. Therefore, the type of average mechanism and the relative strength between the involved scattering mechanisms can be well described by this model. In fact, since the X2-Bragg model, like the original X-Bragg, accounts for depolarization in the surface scattering, it is able to properly describe the presence of nonpolarized returns through the β_1 parameter (roughness measure). The fitting of the X2-Bragg to the measured PR indicates that there exists an important contribution of nonpolarized mechanisms (β_1 values are different from zero, i.e., pure Bragg). Comparatively, the X-Bragg model tends to produce an overestimation of the roughness (β_1) mainly due to the noise contribution. It has been also recognized that the fully polarimetric data can be exploited to apply an additive NF; otherwise, an overestimation of the PR and thus the roughness for both models is expected.

In summary, the study here presented shows that experimental quad-pol TSX acquisitions over the ocean have intrinsic system/scenario limitations (noise and temporal decorrelation), which should be carefully analyzed to avoid an erroneous interpretation of the polarimetric data. This paper sets the theoretical and analytical foundations to extrapolate the inclusion of such impacts to other physical-based scattering models, evaluating their effectiveness with experimental quad-pol data from current state-of-the-art polarimetric SAR sensors.

APPENDIX A
X2-BRAGG DERIVATION

In the following lines, an extension of the X-Bragg model, referred as X2-Bragg, is presented to introduce the impact of both noise and additional temporal decorrelations, in a two-step procedure.

First of all, let us define an equivalent coherency matrix, which accounts for the noise perturbation as (analogous to the study in [19])

$$\mathbf{T}' = \mathbf{T} + \mathbf{N} \tag{8}$$

where $\mathbf{T}$ refers to the expected coherency matrix related to the sea clutter, and the noise coherency matrix is diagonal $\mathbf{N} = \sigma_n^2 \mathbf{I}_{3\times 3}$. For simplicity, it has been assumed that the different polarimetric channels have uncorrelated additive circular complex Gaussian noise with the same power σ_n^2.

From the previous considerations, and using a general formulation, (8) can be expressed as

$$\mathbf{T}' = \left(\sigma_1^2 + \sigma_n^2\right) \overline{\mathbf{T}}' \tag{9}$$

where the normalized (to $\mathbf{T}'_{11}$) coherency matrix $\overline{\mathbf{T}}'$ is written as

$$\overline{\mathbf{T}}' = \begin{bmatrix} 1 & \sqrt{\frac{\sigma_2^2}{\sigma_1^2}} \overbrace{\rho_{\mathrm{SNR}_1}\rho_{12}}^{\rho_T} & 0 \\ \sqrt{\frac{\sigma_2^2}{\sigma_1^2}}\rho_{\mathrm{SNR}_1}\rho_{12}^* & \frac{\sigma_2^2}{\sigma_1^2}\frac{1+1/\mathrm{SNR}_2}{1+1/\mathrm{SNR}_1} & 0 \\ 0 & 0 & \frac{\sigma_3^2}{\sigma_1^2}\frac{1+1/\mathrm{SNR}_3}{1+1/\mathrm{SNR}_1} \end{bmatrix} \tag{10}$$

where σ_1^2, σ_2^2, and σ_3^2 refer to the signal power of the three polarimetric channels (in the Pauli base); SNR_1, SNR_2, and SNR_3 are the corresponding SNRs, i.e., $\mathrm{SNR}_i = \sigma_i^2/\sigma_n^2$; ρ_{12} represents the polarimetric correlation (coherence) coefficient between $(S_{\mathrm{HH}} + S_{\mathrm{VV}})$ and $(S_{\mathrm{HH}} - S_{\mathrm{VV}})$ channels; and ρ_{SNR_1} models the decorrelation effect induced by the presence of thermal noise, i.e.,

$$\rho_{\mathrm{SNR}_1} = \frac{1}{1 + 1/\mathrm{SNR}_1} \tag{11}$$

such that the total coherence, based on a multiplicative model, is defined as ρ_T.

From the original X-Bragg model formulation in (7), the different parameters in (10) can be expressed as

$$\begin{aligned} \sigma_1^2 &= m_s^2 C_1 \\ \sigma_2^2 &= m_s^2 C_3 \left(1 + \mathrm{sinc}(4\beta_1)\right) \\ \sigma_3^2 &= m_s^2 C_3 \left(1 - \mathrm{sinc}(4\beta_1)\right) \\ \rho_{12} &= \frac{C_2 \mathrm{sinc}(2\beta_1)}{\sqrt{C_1 C_3 \left(1 + \mathrm{sinc}(4\beta_1)\right)}}. \end{aligned} \tag{12}$$

From the previous relationships, the three polarimetric SNRs can be defined in terms of an equivalent $\mathrm{SNR}_{\mathrm{Eq}}$ as

$$\begin{aligned} \mathrm{SNR}_1 &= C_1 \mathrm{SNR}_{\mathrm{Eq}} \\ \mathrm{SNR}_2 &= C_3 \left(1 + \mathrm{sinc}(4\beta_1)\right) \mathrm{SNR}_{\mathrm{Eq}} \\ \mathrm{SNR}_3 &= C_3 \left(1 - \mathrm{sinc}(4\beta_1)\right) \mathrm{SNR}_{\mathrm{Eq}} \end{aligned} \tag{13}$$

in a way that, if SNR_1 is estimated from the data, the equivalent $\mathrm{SNR}_{\mathrm{Eq}} = m_s^2/\sigma_n^2$ can be inverted from the model and used to properly account for the thermal noise impact in the X-Bragg model fitting.

In multichannel adaptive array and GMTI theory, the impact of temporal decorrelation is known to cause an increase in the number of eigenvalues (of the clutter-plus-noise covariance matrix) different from the noise floor [3]. The X-Bragg model has been further extended to account for temporal decorrelation, in terms of an additional coherence coefficient ρ_{temp}. It must be noted that this term cannot be directly introduced in matrix (10) since, from the DRA acquisition itself, the temporal decorrelation is between the individual polarimetric channels with some spatial or temporal baseline. This additional term should be considered in the covariance matrix $\mathbf{C}$ formulation. First, a transformation of the normalized coherency matrix $\overline{\mathbf{T}}'$ (10) into the covariance matrix is performed as

$$\overline{\mathbf{C}}' = \left\{\mathbf{U}_{3(\mathrm{L}\to\mathrm{P})}\right\}^{-1} \overline{\mathbf{T}}' \left\{\mathbf{U}_{3(\mathrm{L}\to\mathrm{P})}^H\right\}^{-1} \tag{14}$$

where the unitary transformation $(\mathrm{L} \to \mathrm{P})$ from the lexicographic target vector to the Pauli vector is

$$\mathbf{U}_{3(\mathrm{L}\to\mathrm{P})} = \frac{1}{\sqrt{2}} \begin{bmatrix} 1 & 0 & 1 \\ 1 & 0 & -1 \\ 0 & \sqrt{2} & 0 \end{bmatrix}. \tag{15}$$

Then, the additional coherence coefficient ρ_{temp} is included as multiplicative term into the off-diagonal terms of $\overline{\mathbf{C}}'$ to obtain $\overline{\mathbf{C}}''$. The normalized coherency matrix for the X2-Bragg model

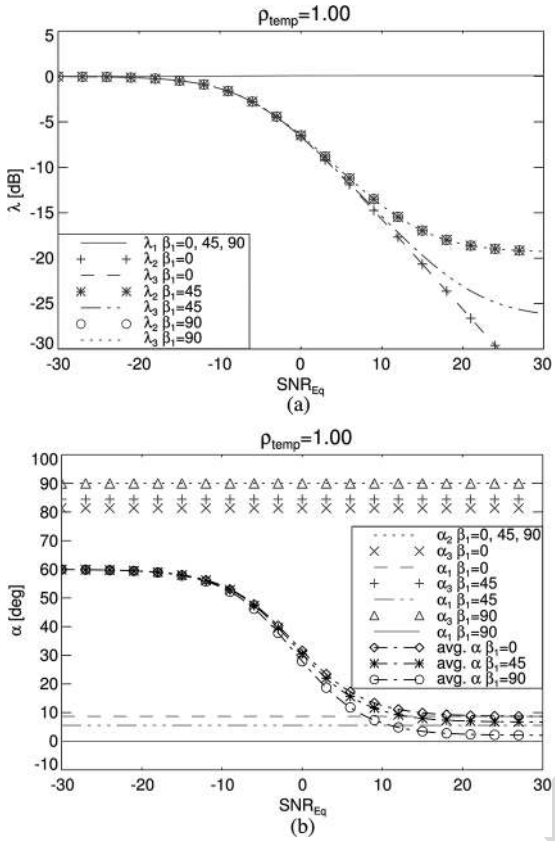

Fig. 11. Sensitivity w.r.t. $\mathrm{SNR_{Eq}}$ for the X2-Bragg model considering the noise impact and a temporal decorrelation $\rho_{\mathrm{temp}} = 1.0$ for three values of the uniform distribution width β_1; an X-band system (9.65 GHz), an incidence angle $\gamma = 24.6°$, a sea temperature of 10 °C, and salinity of 35‰ are considered. (a) Eigenvalues. (b) Alphas.

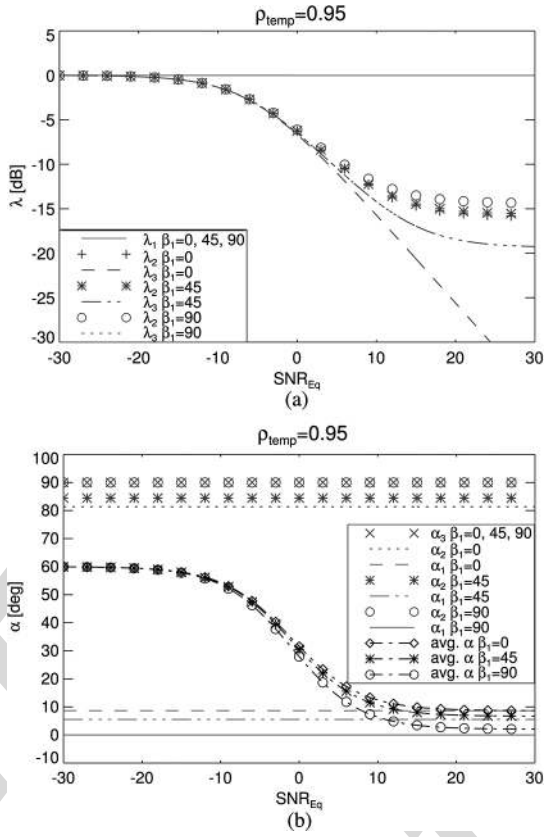

Fig. 12. Sensitivity w.r.t. $\mathrm{SNR_{Eq}}$ for the X2-Bragg model considering the noise impact and a temporal decorrelation $\rho_{\mathrm{temp}} = 0.95$ for three values of the uniform distribution width β_1; an X-band system (9.65 GHz), an incidence angle $\gamma = 24.6°$, a sea temperature of 10 °C, and salinity of 35‰ are considered. (a) Eigenvalues. (b) Alphas.

$\overline{\mathbf{T}}''$ can be obtained using a matrix transformation of $\overline{\mathbf{C}}''$ by means of $\mathbf{U}_{3(\mathrm{L}\to\mathrm{P})}$, inversely analogous to the case in (14).

APPENDIX B
X2-BRAGG THEORETICAL EVALUATION

The sensitivity of the eigenvalues and α parameters as a function of $\mathrm{SNR_{Eq}}$ for $\rho_{\mathrm{temp}} = 1.0$ and $\rho_{\mathrm{temp}} = 0.95$ is shown, respectively, in Figs. 11 and 12, exploiting the theoretical coherency matrix formulation $\overline{\mathbf{T}}''$ of the X2-Bragg model. It has been assumed an X-band system (9.65 GHz), an incidence angle γ of 24.6° [corresponding to the center of TSX-4 acquisition (see Table I)], and sea conditions of 10 °C and 35‰ salinity content. In Figs. 11(a) and 12(a), the eigenvalue distribution is represented as a function of $\mathrm{SNR_{Eq}}$. The three eigenvalues collapse, regardless of β_1 and ρ_{temp}, when reducing $\mathrm{SNR_{Eq}}$ (< -10 dB), being the noise the dominant mechanism.

In case of $\beta_1 = 0°$ (smooth surface) and with increasing $\mathrm{SNR_{Eq}}$, the two smallest eigenvalues λ_2 (plus symbols) and λ_3 (dashed line) have the same decreasing trend when no temporal decorrelation is included [see Fig. 11(a)]. Their contribution is 30 dB below λ_1 for $\mathrm{SNR_{Eq}} > 20$ dB, in which case SPM applies with a single dominant mechanism. This can be observed also from the averaged value $\overline{\alpha}$ [dash–dot line with diamond markers in Fig. 11(b)], which tends to α_1 (dashed line). As β_1 (roughness) increases, the cross-polar power increases; hence, more than a single dominant mechanism exist. For $\beta_1 = 45°$ and $\mathrm{SNR_{Eq}} > 10$ dB, the two smallest eigenvalues (asterisk symbols and dash–dot–dot line) start to diverge. In the limit $\beta_1 = 90°$ and with no additional temporal decorrelation, λ_2 (circle markers) and λ_3 (dotted line) have the same trend as a function of the effective SNR, since polarimetric coherence ρ_{12} decreases to 0. Considering a temporal decorrelation of the sea $\rho_{\mathrm{temp}} = 0.95$, a general increase of the second eigenvalue can be recognized (for $\mathrm{SNR_{Eq}} > 10$ dB), comparing Figs. 11(a) and 12(a), particularly for $\beta_1 = 0°$. In case of λ_3, this behavior is also observed, but for $\beta_1 \geq 45°$.

Contrary to the eigenvalues, the individual α parameters are almost unaffected by the presence of noise, as shown in Figs. 11(b) and 12(b). Polarimetric decomposition considers the mean $\overline{\alpha}$, based on proper weighting of the individual α terms through the eigenvalues' probabilities [14]. As shown in Figs. 11(b) and 12(b), the average $\overline{\alpha}$ presents a large variation as a function of $\mathrm{SNR_{Eq}}$ for different values of β_1. In the limit, $\overline{\alpha}$ tends to 60°, such that the scattering mechanism lies in the extreme edge of region 2 of the Cloude–Pottier $H/\overline{\alpha}$, i.e., random noise, that is, no polarization dependence. Temporal decorrelation exchanges the behavior of the individual α_2 and α_3 parameters, comparing Figs. 11(b) and 12(b), but does not affect the averaged values: when no temporal decorrelation

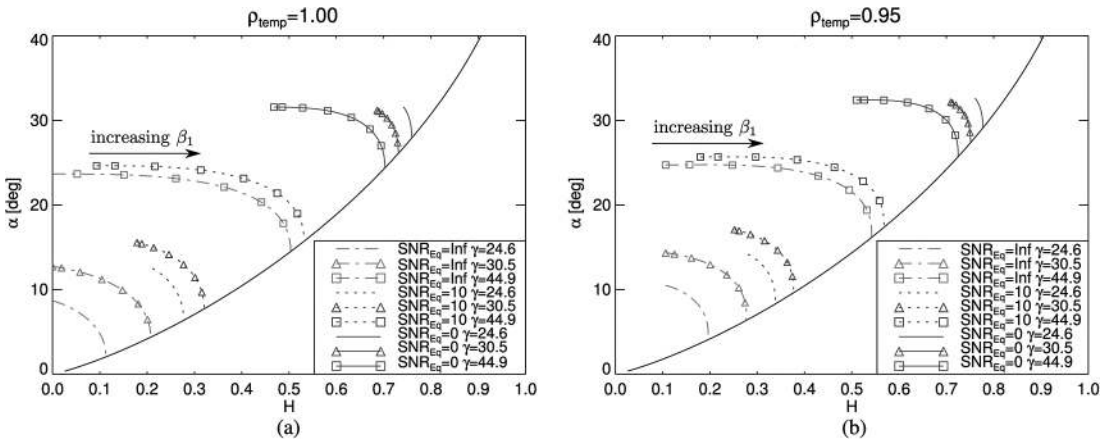

Fig. 13. $H/\overline{\alpha}$ plane for the X2-Bragg model at three incidence angles (24.6°, 33.8°, and 44.9°) and for three $\mathrm{SNR}_{\mathrm{Eq}}$ conditions (∞, 10 dB, and 0 dB): (a) $\rho_{\mathrm{temp}} = 1.0$ and (b) $\rho_{\mathrm{temp}} = 0.95$ (sea water with salinity content of 35‰ and temperature of 10 °C).

is considered ($\rho_{\mathrm{temp}} = 1$), α_2 collapses to 90° regardless of β_1, and α_3 sweeps the values from 80° to 90°, whereas for $\rho_{\mathrm{temp}} = 0.95$, α_3 is 90° for the different roughness parameters. Therefore, temporal decorrelation is not impairing the values of α parameters, but it is modulating the contribution of the different mechanisms, i.e., for $\rho_{\mathrm{temp}} = 0.95$, the cross-polar component (related to $\alpha = 90$ independently from β_1) is no longer the second dominant scattering mechanism (as for $\rho_{\mathrm{temp}} = 1$).

The impact of both thermal noise and temporal decorrelation in the X2-Bragg model is also analyzed in the $H/\overline{\alpha}$ plane, as represented in Fig. 13(a) and (b) for $\rho_{\mathrm{temp}} = 1$ and $\rho_{\mathrm{temp}} = 0.95$, respectively. Different incidence angles, corresponding to the center of data takes TSX-4 (24.6°), TSX-7 (30.5°), and TSX-17 (44.9°), are considered. The noise impact is translated into a progressive increase of both $\overline{\alpha}$ and H as $\mathrm{SNR}_{\mathrm{Eq}}$ decreases. Moreover, the variation of the $H/\overline{\alpha}$ pairs as a function of β_1 is reduced when the noise contribution increases. Temporal decorrelation produces similar effects, but its impact reduces as long as the entropy increases, clearly visible for the region with $H > 0.6$ when comparing Fig. 13(a) and (b).

A particular case in the $H/\overline{\alpha}$ plane is recognized for $\mathrm{SNR}_{\mathrm{Eq}} = 0$ dB, where the variation as a function of the incidence angle is reversed, i.e., the near range presents higher entropy values than the far range: as long as the noise contribution increases, the divergence between the two smallest eigenvalues (λ_2 and λ_3) reduces (increasing the entropy), and this effect is more severe for the near range. This relative separation is also a function of the roughness (β_1), which, for noisy near range scenarios, is quite flat. Such a response justifies the reduction on H as a function of β_1 for increasing noise, particularly at near range.

ACKNOWLEDGMENT

The authors would like to thank the German Aerospace Center (DLR) and, in particular, S. Baumgartner for the TSX quad-pol data provided in the frame of the DRA proposal MTH1971 and the FP7-SPACE Project NEREIDS Ref. 263468 for the TSX dual-pol data. The authors would also like to thank A. Gómez for her helpful suggestions and comments.

REFERENCES

[1] S. Hasselmann, C. Brüning, K. Hasselmann, and P. Heimbach, "An improved algorithm for the retrieval of ocean wave spectra from synthetic aperture radar image spectra," *J. Geophys. Res., Oceans*, vol. 101, no. C7, pp. 16 615–16 629, Jul. 1996.

[2] R. Goldstein and H. Zebker, "Interferometric radar measurement of ocean surface currents," *Nature*, vol. 328, no. 6132, pp. 707–709, Aug. 1987.

[3] E. Makhoul, A. Broquetas, J. Ruiz-Rodon, Y. Zhan, and F. Ceba, "A performance evaluation of SAR-GMTI missions for maritime applications," *IEEE Trans. Geosci. Remote Sens.*, vol. 53, no. 5, pp. 2496–2509, May 2015.

[4] M. Gabele *et al.*, "Fore and aft channel reconstruction in the TerraSAR-X dual receive antenna mode," *IEEE Trans. Geosci. Remote Sens.*, vol. 48, no. 2, pp. 795–806, Feb. 2010.

[5] I. Hajnsek, E. Pottier, and S. Cloude, "Inversion of surface parameters from polarimetric SAR," *IEEE Trans. Geosci. Remote Sens.*, vol. 41, no. 4, pp. 727–744, Apr. 2003.

[6] X.-M. Li and S. Lehner, "Algorithm for sea surface wind retrieval from TerraSAR-X and TanDEM-X data," *IEEE Trans. Geosci. Remote Sens.*, vol. 52, no. 5, pp. 2928–2939, May 2014.

[7] T. Fritz and M. Eineder, "TerraSAR-X: Ground segment basic product specification document," German Aerosp. Center (DLR), Köln, Germany, Tech. Rep. TX-GS-DD-3302, Oct. 2013.

[8] K. D. Ward, R. J. Tough, and S. Watts, *Sea Clutter: Scattering, the K Distribution and Radar Performance*. Stevenage, U.K.: The Insti. Eng. Technol., 2006.

[9] S. Anfinsen and T. Eltoft, "Application of the matrix-variate Mellin transform to analysis of polarimetric radar images," *IEEE Trans. Geosci. Remote Sens.*, vol. 49, no. 6, pp. 2281–2295, Jun. 2011.

[10] S. Skrunes, C. Brekke, T. Eltoft, and V. Kudryavtsev, "Comparing near-coincident C- and X-band SAR acquisitions of marine oil spills," *IEEE Trans. Geosci. Remote Sens.*, vol. 53, no. 4, pp. 1958–1975, Apr. 2015.

[11] E. Jakeman and P. N. Pusey, "A model for non-Rayleigh sea echo," *IEEE Trans. Antennas Propag.*, vol. AP-24, no. 6, pp. 806–814, Nov. 1976.

[12] K. Ouchi and R. Cordey, "Statistical analysis of azimuth streaks observed in digitally processed CASSIE imagery of the sea surface," *IEEE Trans. Geosci. Remote Sens.*, vol. 29, no. 5, pp. 727–735, Sep. 1991.

[13] D. Trizna, "Statistics of low grazing angle radar sea scatter for moderate and fully developed ocean waves," *IEEE Trans. Antennas Propag.*, vol. 39, no. 12, pp. 1681–1690, Dec. 1991.

[14] S. Cloude and E. Pottier, "An entropy based classification scheme for land applications of polarimetric SAR," *IEEE Trans. Geosci. Remote Sens.*, vol. 35, no. 1, pp. 68–78, Jan. 1997.

[15] V. Kudryavtsev, D. Hauser, G. Caudal, and B. Chapron, "A semiempirical model of the normalized radar cross-section of the sea surface 1. Background model," *J. Geophys. Res., Oceans*, vol. 108, no. C3, pp. FET 2-1–FET 2-24, Mar. 2003.

[16] J. Morris, S. Anderson, and S. Cloude, "A study of the X-band entropy of breaking ocean waves," in *Proc. IEEE IGARSS*, Jul. 2003, vol. 2, pp. 711–713.

[17] D. A. Gagliardini and P. C. Colón, "Ocean feature detection using microwave backscatter and sun glint observations," *Gayana (Concepción)*, vol. 68, no. 2, pp. 180–185, 2004.

[18] AIRBUS, "Radiometric calibration of TerraSAR-X data: Beta naught and sigma naught coefficient calculation," AIRBUS Defence Space, Munich, Germany, Tech. Rep. TSXX-ITD-TN-0049, Mar. 2014.
[19] C. López-Martínez, A. Alonso-González, and X. Fabregas, "Perturbation analysis of eigenvector-based target decomposition theorems in radar polarimetry," *IEEE Trans. Geosci. Remote Sens.*, vol. 52, no. 4, pp. 2081–2095, Apr. 2014.
[20] V. Gregers-Hansen and R. Mital, "An improved empirical model for radar sea clutter reflectivity," *IEEE Trans. Aerosp. Electron. Syst.*, vol. 48, no. 4, pp. 3512–3524, Oct. 2012.
[21] F. E. Nathanson, J. P. Reilly, and M. N. Cohen, *Radar Design Principles: Signal Processing and the Environment*, 2nd ed. New York, NY, USA: McGraw-Hill, 1990.
[22] M. Menon, "Estimation of the shape and scale parameters of the Weibull distribution," *Technometrics*, vol. 5, no. 2, pp. 175–182, May 1963.
[23] D. Iskander and A. Zoubir, "Estimation of the parameters of the K-distribution using higher order and fractional moments [radar clutter]," *IEEE Trans. Aerosp. Electron. Syst.*, vol. 35, no. 4, pp. 1453–1457, Oct. 1999.
[24] D. Blacknell and R. J. A. Tough, "Parameter estimation for the K-distribution based on [z log(z)]," *Proc. Inst. Elect. Eng.—Radar Sonar Navig.*, vol. 148, no. 6, pp. 309–312, Dec. 2001.
[25] R. J. A. Tough, D. Blacknell, and S. Quegan, "A statistical description of polarimetric and interferometric synthetic aperture radar data," *Proc. R. Soc. Lond. A, Math. Phys. Sci.*, vol. 449, no. 1937, pp. 567–589, Jun. 1995.
[26] D. Schuler and J. Lee, "Mapping ocean surface features using biogenic slick-fields and SAR polarimetric decomposition techniques," *Proc. Inst. Elect. Eng.—Radar Sonar Navig.*, vol. 153, no. 3, pp. 260–270, Jun. 2006.
[27] M. Migliaccio, A. Gambardella, and M. Tranfaglia, "SAR polarimetry to observe oil spills," *IEEE Trans. Geosci. Remote Sens.*, vol. 45, no. 2, pp. 506–511, Feb. 2007.
[28] A. Voronovich and V. Zavorotny, "Theoretical model for scattering of radar signals in Ku-and C-bands from a rough sea surface with breaking waves," *Waves Random Media*, vol. 11, no. 3, pp. 247–269, 2001.
[29] A. A. Mouche, D. Hauser, and V. Kudryavtsev, "Radar scattering of the ocean surface and sea-roughness properties: A combined analysis from dual-polarizations airborne radar observations and models in C band," *J. Geophys. Res., Oceans*, vol. 111, no. C9, Sep. 2006, Art. ID. C09004.
[30] D. Schuler, J.-S. Lee, and K. Hoppel, "Polarimetric SAR image signatures of the ocean and gulf stream features," *IEEE Trans. Geosci. Remote Sens.*, vol. 31, no. 6, pp. 1210–1221, Nov. 1993.
[31] L. Klein and C. Swift, "An improved model for the dielectric constant of sea water at microwave frequencies," *IEEE Trans. Antennas Propag.*, vol. AP-25, no. 1, pp. 104–111, Jan. 1977.
[32] R. Romeiser and D. Thompson, "Numerical study on the along-track interferometric radar imaging mechanism of oceanic surface currents," *IEEE Trans. Geosci. Remote Sens.*, vol. 38, no. 1, pp. 446–458, Jan. 2000.

Eduardo Makhoul (S'09–M'15) was born in Homs, Siria, in 1985. He received the M.Sc. degree in electrical engineering and the Ph.D. degree (*cum laude*) from Universitat Politècnica de Catalunya (UPC), Barcelona, Spain, in 2009 and 2015, respectively.

In 2008, he worked on his master thesis in the frame of high-resolution wide-swath synthetic aperture radar (SAR) systems at the German Aerospace Center (DLR). In 2009, he joined the Remote Sensing Laboratory, UPC, researching on aspects of ground moving target indication (GMTI) for future spaceborne SAR systems. From 2009 to 2011, he worked on the radiometric budget analysis of the Spanish mission PAZ. From 2010 to 2013, he worked on the analysis and study of SAR-GMTI systems and techniques for future European missions in the frame of NEWA and SIMTISYS projects. In 2013 (April–August), he was a Visiting Researcher with DLR, working on SAR-GMTI processing of airborne and spaceborne data over maritime scenarios. Since August 2015, he has been with IsardSAT, an experienced Earth observation research company in Barcelona, involved in the design, calibration, and maintenance of civil remote sensing instruments. His main research interests include SAR, GMTI, radar system design, mission performance, calibration, array signal processing, sea/ocean surveillance, and polarimetry.

Carlos López-Martínez (S'97–M'04–SM'11) received the M.Sc. degree in electrical engineering and the Ph.D. degree from Universitat Politècnica de Catalunya (UPC), Barcelona, Spain, in 1999 and 2003, respectively.

From October 2000 to March 2002, he was with the Frequency and Radar Systems Department, HR, German Aerospace Center (DLR), Oberpfaffenhofen, Germany. From June 2003 to December 2005, he was with the Image and Remote Sensing Group SAPHIR Team of the Institute of Electronics and Telecommunications of Rennes (IETR CNRS UMR 6164), Rennes, France. In January 2006, he joined UPC, Barcelona, as a Ramón y Cajal Researcher. He is currently an Associate Professor in the area of remote sensing and microwave technology with UPC. He has authored or coauthored over 100 articles in journals, books, and conference proceedings in the radar remote sensing and image analysis literature. His research interests include SAR and multidimensional SAR, radar polarimetry, physical parameter inversion, digital signal processing, estimation theory, and harmonic analysis.

Dr. López-Martínez is an Associate Editor of the IEEE JOURNAL OF SELECTED TOPICS IN APPLIED EARTH OBSERVATIONS AND REMOTE SENSING. He served as a Guest Editor of the *EURASIP Journal on Advances in Signal Processing*. He has organized different invited sessions in international conferences on radar and SAR polarimetry. He has presented advanced courses and seminars on radar polarimetry to a wide range of organizations and events. He was a recipient of the Student Prize Paper Award at the EUSAR 2002 Conference and coauthored the paper awarded with the First Place Student Paper Award at the EUSAR 2012 Conference. He has been also a recipient of the IEEE Geoscience and Remote Sensing Society 2013 GOLD Early Career Award.

Antoni Broquetas (S'84–M'90) was born in Barcelona, Spain, in 1959. He received the Ingeniero degree in telecommunications engineering and the Doctor Ingeniero degree in telecommunications engineering (for his work on microwave tomography) from Universitat Politècnica de Catalunya (UPC), Barcelona, in 1985 and 1989, respectively.

In 1986, he was a Research Assistant with Portsmouth Polytechnic, Portsmouth, U.K., involved in propagation studies. In 1987, he joined the Department of Signal Theory and Communications (TSC), UPC, where he was the Subdirector of Research of the Institute of Geomatics from 1998 to 2002 and the Director of TSC from 2003 to 2006. Since 1999, he has been a Full Professor with UPC, involved in research on radar imaging and remote sensing. He has authored or coauthored over 150 papers on microwave tomography, radar, ISAR and SAR systems, and SAR processing and interferometry.

AUTHOR QUERIES

AUTHOR PLEASE ANSWER ALL QUERIES

Please be aware that authors are required to pay overlength page charges ($200 per page) if the paper is longer than 6 pages. If you cannot pay any or all of these charges please let us know.

This pdf contains 2 proofs. The first half is the version that will appear on Xplore. The second half is the version that will appear in print. If you have any figures to print in color, they will be in color in both proofs.

The "Open Access" option for your paper expires when the paper is published on Xplore in an issue with page numbers. Papers in "Early Access" may be changed to "Open Access."

AQ1 = Please check if changes made in the affiliation of author E. Makhoul are correct. Otherwise, please make the necessary changes.
AQ2 = Please provide the expanded form of "DFO."

END OF ALL QUERIES